

# AIRSAR Along-Track Interferometry Data

David A. Imel\*

Jet Propulsion Laboratory 300-243  
4800 Oak Grove Drive, Pasadena, CA 91109

AIRSAR Earth Science and Applications Workshop  
4–6 March 2002

## 1 Introduction

In Along-Track Interferometric (ATI) data<sup>1</sup> the interferometric phase at each pixel is related to the motion of the scatterers within the pixel. ATI (See Figure 1.) mode data has been collected by the AIRSAR instrument as early as 1987—originally as a classified experiment. Although a few ATI data sets have been published, in each case the processing was experimental and each data set required significant “special processing” because of the immaturity of both the motion measurement system available and the state of interferometric SAR processing. We have since acquired a much more accurate embedded GPS/INU system and have gained experience in interferometric SAR processing which we have applied to the development of an operational ATI processor.

### 1.1 Why ATI?

There are several advantages of ATI data over conventional radar and other existing oceanographic monitoring systems. Some of these advantages and applications of ATI include:

- ATI (unlike altimetry, for example) provides a direct measurement of the surface velocity—no geostrophic assumption is required.
- Ocean signatures of boundary layers are much greater in the phase than in the brightness of a radar return, since the backscatter tends to be proportional to wave-height while phase is proportional to wave direction and speed.

---

\* [imel@jpl.nasa.gov](mailto:imel@jpl.nasa.gov)

<sup>1</sup>For the convenience of the reader, an abbreviated Bibliography is provided at the conclusion of this paper.

- With an ATI system the coherence time is measured directly and may be useful for monitoring micro wave-breaking events which control the ocean-atmosphere gas transport/mixing process.
- Wave spectra measured by the ATI phase are less distorted than those obtained by brightness imagery alone.
- ATI data may provide enhanced indication of man-made moving targets, with significant slower minimum detectable velocities than conventional moving-target radars.
- ATI data may be useful for mapping surfactant and pollution dispersion paths.
- ATI data can be used to map coastal surf-zones, identifying areas of heavier surf or relatively protected shores.

## 1.2 Concept

As an electromagnetic wave propagates a round-trip distance  $2\rho$  to and from a scatterer its phase changes by

$$\phi = -\frac{4\pi}{\lambda}\rho \quad (1)$$

due to the propagation, where  $\lambda$  is the wavelength of the radiation and the sign is given by noting that the doppler shift due to a scatterer with a range changing in time is:

$$f_D = \frac{1}{2\pi} \frac{d\phi}{dt} = -\frac{2}{\lambda} \dot{\rho} \quad (2)$$

where  $\dot{\rho}$  is the time rate of change of the propagation distance, i.e., a “blue-shift” as the scatterer approaches the radar and a “red-shift” as it recedes. The ATI phase is formed at each pixel in an image by a conjugate-multiply of the first image ( $C_1$ ) by the second ( $C_2$ ), i.e.,

$$\Delta\phi = \arg(C_1 C_2^*). \quad (3)$$

For a scatterer moving at a velocity  $\mathbf{u}$  and a radar with a line of sight to the target,  $\mathbf{n}$  the change in phase is

$$\Delta\phi \approx \frac{4\pi}{\lambda} \mathbf{n} \cdot \mathbf{u} \Delta t \quad (|\mathbf{u}| \Delta t \ll \rho) \quad (4)$$

where  $\Delta t$  is the time between two consecutive observations. This is the phase measured in an along-track interferometric SAR.

Note that we have assumed that the signal propagates to the scatterer and back at from the same location. It is important that the spatial interferometric baseline for ATI data is zero—the only baseline is temporal. Ideally, one would use an array of large stationary antennas to map the phase,  $\Delta\phi$  of a scene. This

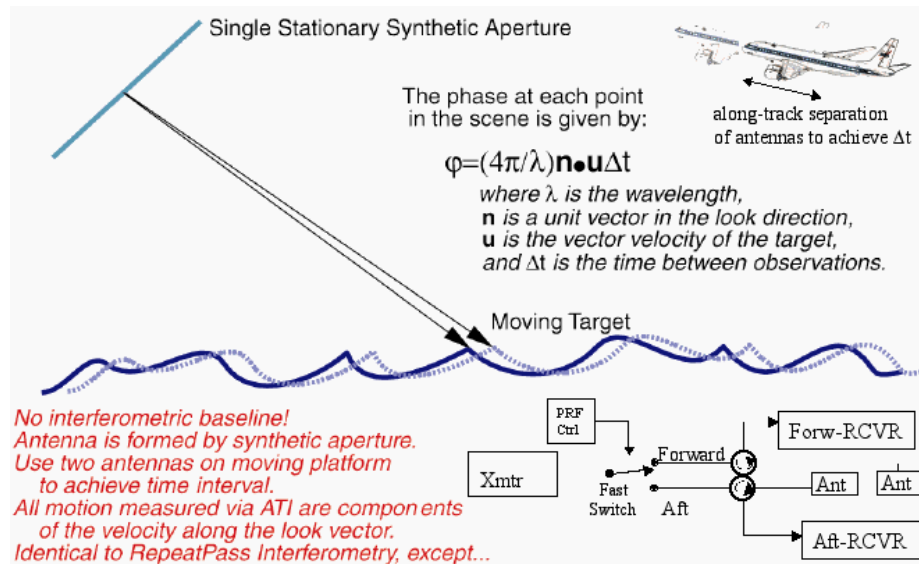


Figure 1: Figure portraying the concept of along-track interferometry. In ATI, the ideal spatial baseline is zero—the only baseline should be a temporal one. In order to acquire two synthetic apertures spaced a short time apart, two antennas are displaced on the platform along the direction of motion. This is the same concept as repeat-pass interferometry, except that in along-track interferometry the two synthetic apertures are formed in one pass, so that the time interval is very small. The synthetic aperture formed by the first antenna will be acquired a time  $\Delta t = b/v$  before the second, where  $b$  is the separation of the two antennas and  $v$  is the speed of the platform. In repeat-pass interferometry, there is temporal decorrelation which occurs between the passes, but the scene is not usually moving during the formation of the synthetic aperture. In along-track interferometry, which is typically used for measuring ocean currents, the scene decorrelates on the time-scale of the formation of the synthetic aperture.

ATI Mode	$b$	$\Delta t$	$(\mathbf{n} \cdot \mathbf{u})_{\text{amb}}$
LP	19.7 m	99 ms	1.2 m/s
LC	9.8 m	49 ms	2.4 m/s
CP	1.9 m	9.5 ms	3.0 m/s
CC	95 cm	4.8 ms	5.9 m/s

Table 1: The AIRSAR ATI systems. In the mode name, the first letter represents the frequency band and the second, the type of along-track baseline.  $b$  is the “effective” baseline, which is the same as the physical baseline for the “ping-pong” modes, LP and CP, and approximately half of the physical baseline for the “common-transmitter” modes (LC and CC) where only one antenna is used for transmit.  $\Delta t$  is the time interval corresponding to each effective baseline for a platform moving at a nominal speed of 200 m/s. A nominal PRF of 800 Hz is assumed.

is impractical. Instead, we use a pair of SAR antennas displaced in the direction of the travel of a moving platform. If the platform moves at a speed  $v$  and the phase centers of the antennas are displaced a distance  $b$ , then the time interval between the two SAR images formed using the two antennas will be  $\Delta t = b/v$ , assuming that the radar transmits alternately from each antenna, and receives the signal with the same antenna used to transmit (so-called “ping-pong” mode).

There is an important subtlety being overlooked in the above discussion: since we are using a SAR to form each image, each image will be formed by integrating the return over a synthetic aperture of length  $S = \rho\theta$  where  $\theta$  is the antenna beamwidth,  $\theta \approx \lambda/L$ . The time to integrate each image is therefore

$$T = \frac{\rho\lambda}{vL} \quad (5)$$

where  $L$  is the antenna length. This time is on the order of a few seconds for the AIRSAR L and C-band radars, which can be fairly long compared to the correlation time of the ocean. This will be discussed further at the end of the paper. Meanwhile, it is clear that short-timescale oscillatory motions will be averaged out in favor of longer-time scale motion (swell and ocean currents).

### 1.3 AIRSAR ATI Capability

AIRSAR has both L-band and C-band systems. Table 1 details the geometry of these systems, which are illustrated in Figure 2. For a time interval between observations of  $\Delta t$ , the ambiguous velocity component is given by

$$\Delta\phi = -\frac{4\pi}{\lambda}(\mathbf{n} \cdot \mathbf{u})_{\text{amb}}\Delta t = 2\pi \quad (6)$$

The maximum unambiguous velocity components for each AIRSAR ATI system are also given in Table 1.

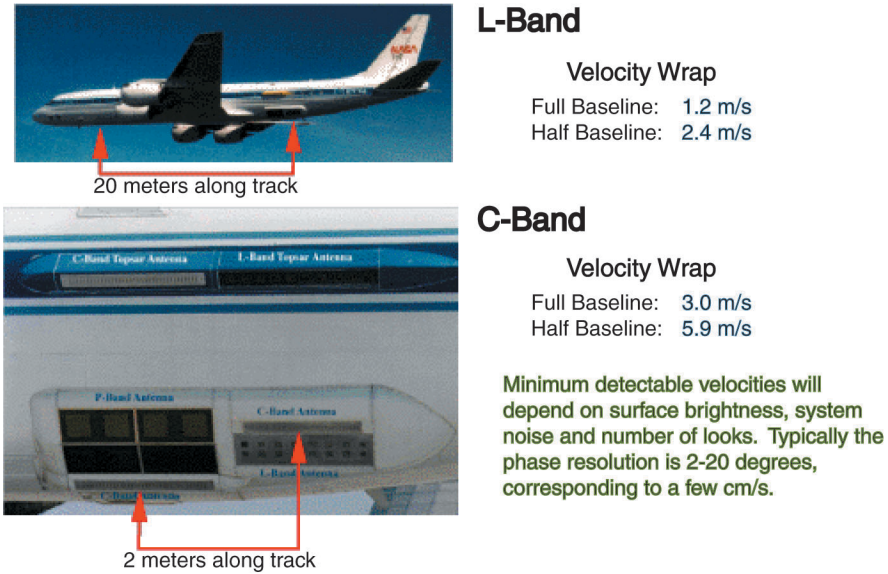


Figure 2: The along-track baselines for both L-band (top image) and C-band (lower image) for the AIRSAR system.

## 2 The AIRSAR ATI Processor

The AIRSAR ATI processor consists of a typical range-doppler front-end SAR processor for image formation, followed by interferogram formation, phase unwrapping (which is typically less important for ocean applications than it would be for a cross-track interferometer, since ocean currents rarely wrap the interferometric phase for the AIRSAR along-track baselines) and geo-location. In this section we highlight some of the details of the AIRSAR ATI processor.

### 2.1 Motion Alignment

A crucial component of the ATI processing is the alignment of the interferometric channels. The trajectory of the phase center of each interferometric channel is determined from the platform motion and attitude data (Figure 3) combined with the lever arms from the embedded GPS/INU to the antenna phase centers. Based on these trajectories, a common reference trajectory (Figure 4) is formed to facilitate image formation. This trajectory is the synthetic antenna aperture. Thus, the signals from each interferometric antenna must be propagated to this reference trajectory. This propagation is carefully accomplished by using an average platform attitude (and therefore, imaging plane) at each point along the reference trajectory. This imaging plane determines from where along the individual phase center trajectories the signals must be propagated to

the reference trajectory.

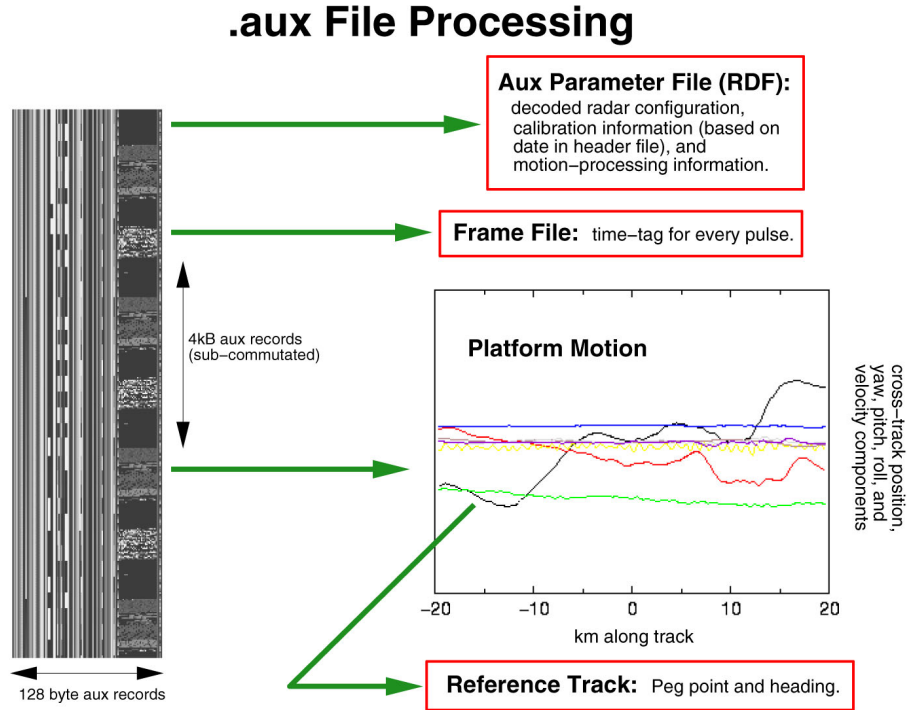


Figure 3: Illustration of the telemetry and processing used as input to the motion alignment algorithm of the ATI processor. On the left is an image of the telemetry, where each byte is represented by a greyscale value. The telemetry uses “fast headers”, i.e., a new value every pulse, for rapidly-changing information such as the aircraft platform. It uses “sub-commutated headers”, i.e., headers where a few bytes are embedded in each “fast header” and many such headers are assembled into a full “sub-commutated header”. These are used for information which changes much less rapidly, such as information about the instrument configuration and site information. The telemetry is decoded into a parameter file used to configure the SAR processor, a motion file describing the platform motion, and a file of time-tags for each individual pulse.

## 2.2 Range Compression

The raw signal data (proportional to the voltage digitized at the analog-to-digital converters after being mixed down to video from microwave frequencies) (Figure 5) is compressed against the reference chirp to localize the time of the return of each scattered signal within a given pulse. The information determined by the previous motion alignment step is then used to interpolate (Figure 6)

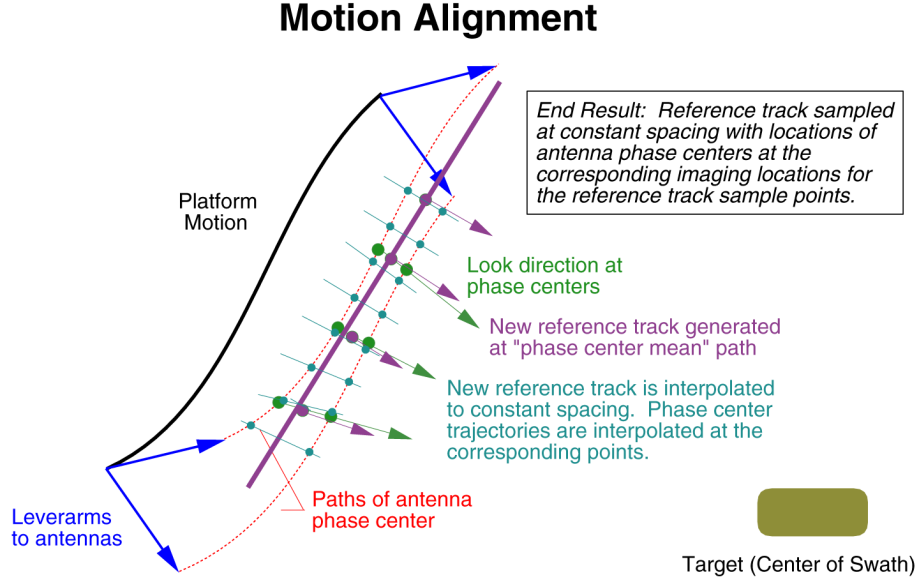


Figure 4: Diagram of the alignment of the two interferometric channels.

the pulses from both interferometric channels to a constant spacing along the reference trajectory to prepare for image formation.

### 2.3 Motion Compensation

The motion compensation of the data relies on the accuracy of the elevation reference, as well as the position information from the embedded GPS/inertial navigation system. In particular, any error in the elevation reference will introduce a phase bias into the data for each channel. In a system with antennas displaced solely along track, this presents no difficulty, because the same phase bias is introduced into each channel and is cancelled in the interferogram. However, where there is a cross-track baseline component as well (as is the case in both AIRSAR ATI radars, but especially the C-band system) this phase bias will be different for each channel, leading to what appears to be a topographic phase signature. This only occurs when the scatterer is at a significantly different elevation than the reference. The motion-compensation correction used to propagate the signal from the antenna phase center to the synthetic array is:

$$\rho_m = \mathbf{l} \cdot \mathbf{n} \quad (7)$$

where  $\mathbf{l}$  is the lever arm to an antenna phase center and  $\mathbf{n}$  is the look direction unit-vector. The propagation is accomplished by an interpolation followed by a phase-correction of  $\phi_m = -(4\pi/\lambda)\rho_m$ . The baseline vector,  $\mathbf{b}$ , is the

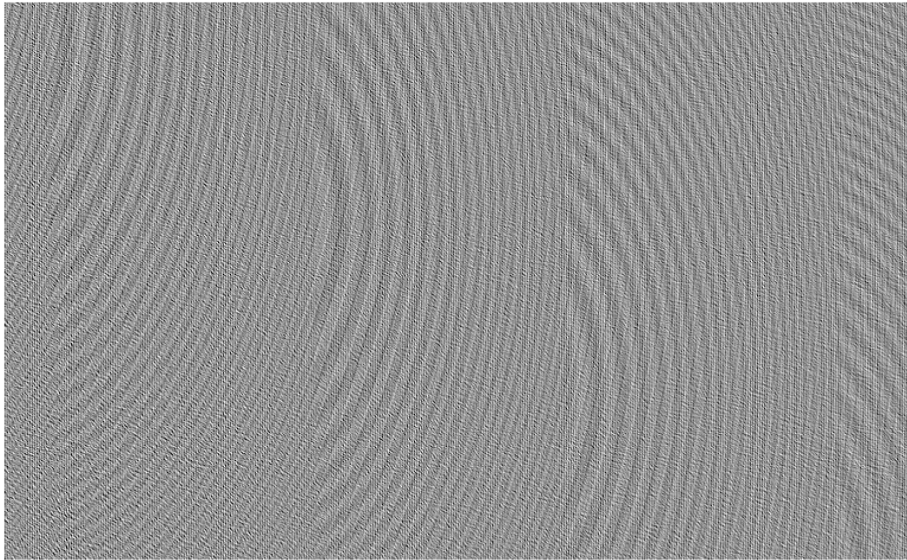
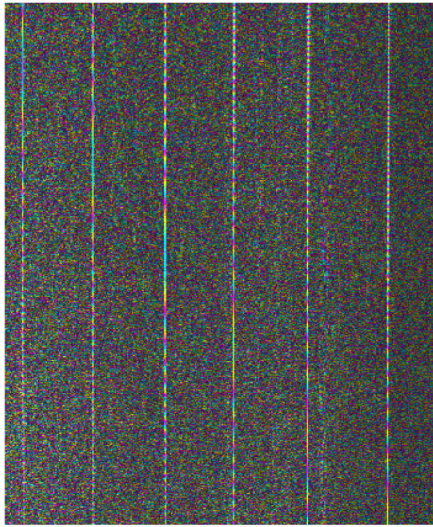


Figure 5: Example radar signal data, where voltages at video have been digitized by the analog-to-digital converters and recorded as bytes. In this image, zero-voltage amplitude is recorded as a medium gray, a high positive voltage is white and a large negative voltage is black. Each row of this image represents one pulse—time increases from top to bottom. The left side is the part of the pulse which returned first, and the right side is the far-range return. (This is just a segment of the total return) This is data over the corner reflector array at Rosamond dry lake bed. The bright “semi-droplets” are the phase history of the corner reflectors, at least four of which are clearly visible in this segment.

## Presumming/Interpolation



- 1) Signal returns are range compressed.
- 2) Doppler (as a function of look angle) is book-kept via motion data.
- 3) Interpolation buffer is filled---one filter-length's worth of pulses at a time. Filter length varies as ratio of resampled pulse spacing to the original pulse spacing along-track.
- 4) Pulses in buffer are base-banded to remove Doppler.
- 5) Pulses are interpolated.
- 6) Doppler shift is re-introduced to interpolated pulses. Phase continuity from pulse-to-pulse is carefully maintained.

Figure 6: Details and illustration of range compression and presumming/interpolation stage of the ATI processor. The image on the left is part of a calibration scene before image formation but after range-compression and presumming/interpolation. The bright lines are point targets (corner-reflectors) which have a phase-history (represented here by color) as they pass through the antenna pattern. A rapidly-changing phase means a large Doppler, while a slowly-changing phase means that the target is either passing through zero-Doppler (i.e., broadside to the radar) or a Doppler ambiguous (in multiples of the resampled pulse-repetition frequency) with zero-Doppler.

difference between the two lever-arm vectors, and the difference in the motion-compensation phase distortion between the two interferometric channels introduced by an error in the elevation reference is:

$$\delta\phi_m = -\frac{4\pi}{\lambda} \mathbf{b} \cdot \frac{\partial \mathbf{n}}{\partial h} \Delta h = -\frac{4\pi \Delta h}{\lambda \rho} \mathbf{b} \cdot [\mathbf{z} + \mathbf{y} \cot \theta] \quad (8)$$

where  $\mathbf{z}$  and  $\mathbf{y}$  are unit vectors in the vertical and cross-track directions, respectively, and  $\theta$  is the look angle. This effect is illustrated in Figure 7, where the typical magnitude of the effect is also described.

This phase does not affect sea-level ATI processing, and is negligible for most sea-states. The topography contribution could be eliminated for all scenes by introducing a digital elevation model to the motion-compensation algorithm.

Motion compensation is performed assuming a constant elevation reference. This is a good assumption for the ocean surface, but introduces phase errors over land:

$$\Delta\phi \approx \frac{4\pi d_z h}{\lambda r}$$

where  $d_z$  is the vertical component of the antenna phase center separation,  $h$  is the altitude of the scatterer above the elevation reference,  $\lambda$  is the wavelength, and  $r$  is the range to the scatterer.

Thus, for PacRim 2000 data, the phase wrap over topographic variations will be:

**C-band: 800-1300 m**

**\*L-band: 6600-10000 m**

Phase error due to 10 m of topography:

**C-band: 5-7 degrees**

**L-band: <0.5 degrees**

(for one degree of pitch)

\*Divided by degrees of pitch

*C-band phase errors are due to a 61 cm vertical baseline, while L-band phase errors are due to pitched 20 m along-track baseline.*

Velocity wrap for upper interferogram is twice that of the lower. Golden Gate Bridge, from EO CAP 1998 data acquisition campaign.

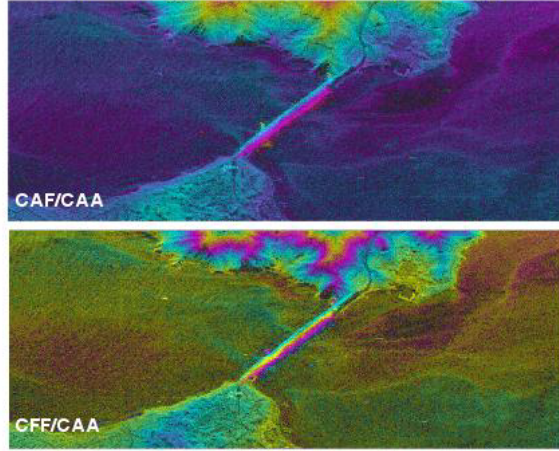


Figure 7: Example and typical magnitude of the topography phase observed in ATI data scenes.

## 2.4 Image Formation

The AIRSAR ATI processor uses the standard (squinted) range-doppler algorithm for image formation, but employs the exact range for the range-migration and azimuth compression steps:

$$\frac{\delta\rho}{\rho} = 1 - \left( \frac{\cos^2 \theta}{\cos^2 \theta_c} \right)^{\frac{1}{2}} \quad (9)$$

where  $\delta\rho$  is the range migration correction,  $\rho$  is the squinted, motion-compensated range to the target. The correction is applied in the frequency domain, so  $\theta$  is the azimuth angle at a given doppler frequency:

$$\sin \theta = \frac{\lambda}{2v} f \quad (10)$$

where  $f$  is the Doppler frequency,  $v$  is the along-track speed of the platform, and  $\lambda$  is the wavelength of the radar.  $\theta_c$  is the azimuth angle at the Doppler centroid.

The azimuth reference function is first computed in the time domain:

$$g(t)e^{-4\pi\rho(t)/\lambda} \quad (11)$$

and then Fourier-transformed to do the convolution as a conjugate-multiply in the doppler-domain.  $g(t)$  is a windowing function to used to reduce azimuth ambiguity noise and limit the reference function to the desired synthetic aperture length. In the examples presented here, the full synthetic aperture is used for  $g(t)$ . A further refinement will be to limit  $g(t)$  to the time specified by (5).

The interferogram is formed from the single-look imagery in the slant range, and the correlation map is formed by averaging the single-look imagery over several looks:

$$\gamma = \frac{\langle C_1 C_2^* \rangle_N}{\sqrt{\langle C_1 C_1^* \rangle_N} \sqrt{\langle C_2 C_2^* \rangle_N}} \quad (12)$$

The magnitude of each element in this map is a number between 0 and 1 and the argument is the interferogram, averaged over  $N$  looks.

## 2.5 Phase Unwrapping

Once the image (and interferogram) formation process is complete, the data are unwrapped by the standard AIRSAR phase-unwrapping program, which also calculates the correlation magnitude image. (The details of the phase unwrapping program are beyond the scope of this paper.)

## 2.6 Geo-location

The interferogram, the correlation magnitude, and the file of incidence angles are projected onto a sea-level elevation reference at a specified post-spacing. The typical post-spacing for 40 MHz bandwidth ATI scenes is 10 meters. The interferometric phases are converted to velocities in the context of this projection. Note that the velocities are **not** projected velocities, but are rather the component of the velocity along the line-of-sight to the radar. This line-of-sight can be obtained everywhere in the scene from the projected incidence angle map which is also generated. Since the absolute phase of the interferograms is still not calibrated at the time of this writing, there will be a global velocity offset which should be removed using either land in the scene or ships with velocities independently obtainable by their along-track displacements and wakes.

There are two ways to accomplish geo-location, or regridding, of ATI data sets. One way is to generate the grid on the ground at the desired post-spacing and for every point in the grid find the corresponding points in the slant-range interferogram and fill the desired point with some average of the interferogram points. The second way is to take each point in the slant-range interferogram and find the nearest points in the grid, filling them each with the value from the interferogram. Each method has advantages and drawbacks, and both are CPU-intensive in the search for mapping from a slant-range image to a ground-range image in the context of a radar with a varying look-direction. The AIRSAR ATI processor uses the first geo-location method described above.

### 3 Calibration

Table 3 describes the parameters used to calibrate AIRSAR ATI data. The following is the calibration procedure for AIRSAR ATI data:

1. Calibration data are acquired over the standard AIRSAR calibration site—the corner reflector array on the Rosamond Dry Lake bed. (See Figure 8. The site has the advantage that all scatterers are moving with a known velocity—zero!
2. The Doppler centroid of the data set is estimated as a function of range from the radar signal data. This is compared to the Doppler centroid predicted by the INU-measured attitude, and used to determine biases for pitch,  $\Delta p$ , and yaw,  $\Delta y$ .

The latter Doppler centroid (phase change per pulse) is calculated from the motion data:

$$\phi_D = \frac{4\pi t_{\text{prf}}}{\lambda} \left\{ \begin{aligned} &v_s \left( \sin y \sin \left[ \cos^{-1} \frac{h \sec p}{\rho} \right] + \frac{h \cos y \tan p}{\rho} \right) + \\ &v_c \left( \cos y \sin \left[ \cos^{-1} \frac{h \sec p}{\rho} \right] - \frac{h \sin y \tan p}{\rho} \right) - \\ &v_h \frac{h}{\rho} \end{aligned} \right\} \quad (13)$$

where  $\phi_D$  is the Doppler,  $t_{\text{prf}}$  is the time between pulses from a given antenna (either forward or rear),  $\lambda$  is the wavelength,  $p$  is pitch,  $y$  is yaw,  $h$  is the height of the platform above the terrain,  $v_s$ ,  $v_c$  and  $v_h$  are the along-track, cross-track and height components of the platform velocity, and  $\rho$  is the slant range.

In order to estimate the bias in yaw and pitch we solve a set of linear equations:

$$\phi_D^{\text{Est}}(\rho_i) = \phi_D^{\text{IMU}}(\rho_i) + \frac{d\phi_D}{dy}(\rho_i)\Delta y + \frac{d\phi_D}{dp}(\rho_i)\Delta p \quad (14)$$

for  $\Delta y$  and  $\Delta p$ , the yaw and pitch biases, respectively; where  $\phi_D^{\text{Est}}(\rho_i)$  are the Doppler centroid estimates from the radar phase history at ranges  $\rho_i$  and similarly,  $\phi_D^{\text{IMU}}(\rho_i)$  are the Doppler centroid calculations from the motion data. (Note that the Doppler centroid may only be estimated from the radar phase history modulo an even number of  $\pi$ 's. These are added back in to make the comparison to the Doppler centroid calculated from the motion data.)  $\frac{d\phi_D}{dy}(\rho_i)$  are the derivatives of the Doppler centroid with respect to yaw evaluated at ranges  $\rho_i$  and similarly,  $\frac{d\phi_D}{dp}(\rho_i)$  are the derivatives of the Doppler centroid with respect to pitch. These derivatives are:

$$\frac{d\phi_D}{dp} = \frac{4\pi t_{\text{prf}}}{\lambda} \left\{ \begin{aligned} &v_s \left( \frac{h \cos y \sec^2 p}{\rho} - \frac{h^2 \sec^2 p \sin y \tan p}{r^2 (1 - (\frac{h \sec p}{\rho})^2)^{\frac{1}{2}}} \right) + \\ &v_c \left( \frac{-h \sec^2 p \sin y}{\rho} - \frac{h^2 \cos y \sec^2 p \tan p}{r^2 (1 - (\frac{h \sec p}{\rho})^2)^{\frac{1}{2}}} \right) \end{aligned} \right\} \quad (15)$$

$$\frac{d\phi_D}{dy} = \frac{4\pi t_{\text{prf}}}{\lambda} \left\{ \begin{aligned} &v_s \left( \cos y \sin \left[ \cos^{-1} \frac{h \sec p}{\rho} \right] - \frac{h \sin y \tan p}{\rho} \right) + \\ &v_c \left( -\sin y \sin \left[ \cos^{-1} \frac{h \sec p}{\rho} \right] - \frac{h \cos y \tan p}{\rho} \right) \end{aligned} \right\} \quad (16)$$

3. An initial image and interferogram is formed for a standard calibration set with corner reflectors in the scene.
4. The ranges to surveyed corner reflectors located in the calibration data set are computed using the platform position information and compared to the ranges at which the corner reflectors appear in the slant-range imagery. The difference between the actual and observed range is the common-range delay,  $r_c$ . (Figure 9)
5. The cross-correlation between the two interferometric channels is used to obtain the differential delay,  $r_d$ , (from the range offset) and a first estimate of a correction to the along-track baseline ( $\mathbf{s} \cdot \Delta \mathbf{b}$ ) (where  $\mathbf{s}$  is a unit vector along the direction of platform motion). (See Figure 10.)
6. Image and interferogram formation is repeated using the updated calibration parameters. The phase variation as a function of range (assuming a stationary calibration scene) is used to fit, and remove, cross-track baseline components: ( $\mathbf{c} \cdot \Delta \mathbf{b}$ ) and ( $\mathbf{h} \cdot \Delta \mathbf{b}$ ), where  $\mathbf{c}$  and  $\mathbf{h}$  are unit vectors in the cross-track and height direction, respectively. These are estimated by solving the set of linear simultaneous equations:

$$A \Delta \mathbf{b} \cdot \mathbf{n} = \eta \quad (17)$$

for  $\Delta \mathbf{b}$  where  $\Delta \mathbf{b}$  is the vector of baseline components errors,  $\eta$  is the vector of interferometric phase observations over the stationary terrain

Parameter	Description
$r_c$	common range delay
$r_d$	differential range delay
$\Delta \mathbf{b}$	baseline correction ( $\Delta(\mathbf{l}_1 - \mathbf{l}_2)$ )
$\Delta p$	INU pitch bias
$\Delta y$	INU yaw bias
$\Delta \phi$	phase offset

Table 2: Each of these parameters is a single constant ( $\Delta b$  has three constant components) which should hold for a given instrumental configuration. In other words, these eight parameters may be determined at the beginning of a data collection campaign over a calibration site and then applied to correct every subsequent data set without re-measurement of the calibration parameters.

(will be zero when the baseline components are correct), the line-of-sight vector is:

$$\mathbf{n} = \begin{pmatrix} \sin y \sin \gamma + \cos y \sin p \cos \gamma \\ \cos y \sin \gamma - \sin y \sin p \cos \gamma \\ -\cos p \cos \gamma \end{pmatrix}; \quad \gamma \equiv \cos^{-1} \frac{h}{\rho \cos p} \quad (18)$$

and the rotation matrix  $A$  is given by the yaw, pitch, roll Euler angle sequence for the INU. (See Figure 11.)

7. A scene with land at a known elevation reference is used to determine the phase offset between the two interferometric channels. This calibration signal phase is used to track phase changes in the receiver chain during the mission.

To date, we have accomplished the baseline and differential delay calibration steps. The absolute phase offset between the two channels is not yet calibrated. This means that some point of known phase (for example, land near the elevation reference or targets with a known velocity) must be used in each scene to get the absolute velocity components. See Figure 12 for a graph of the phase calibration.

Also not determined for the data sets shown in this paper is the yaw and pitch-bias estimation. Such a bias can come from two places:

1. The inertial navigation unit may report attitude angles which have constant offsets. These are typically calibrated out during an alignment procedure at the beginning of a data acquisition campaign. However, there may be some uncertainty in the results of that measurement. A bias in the attitude would lead to errors in the location of the antenna phase centers, multiplied through the lever arms of the antennas. However, since the biases are constant and small, these errors get folded into the estimation of the antenna lever arms themselves. The phase calibration (Figure 12) shows that these errors are small.

2. The antennas may be mounted so that the antenna patterns are not pointed to broadside. These biases, if they are small, can lead to errors in a radiometric calibration, since the processor selects the squint angle to which to process the data based on the motion measurements for each patch. If the squint used to process the data is not the same as that given by the pointing of the antenna pattern, less energy than the maximum will be processed and there can be a radiometric error. Note that ATI data are not currently radiometrically calibrated, so that such an error would not be noticed.

## Corner Reflector Array

Rosamond Dry Lake Bed, California



Figure 8: Standard AIRSAR calibration site: the corner reflector array at the Rosamond dry lake bed. Upper left: the corner reflectors are guyed down to keep them stable. The ground is very smooth at radar wavelengths, making for a dark background to the bright corner reflectors. Upper right: the AIRSAR Engineer, Walter Skotnicki poses next to a corner reflector to give a sense of scale. Lower image: several of the reflectors in the array can be seen.

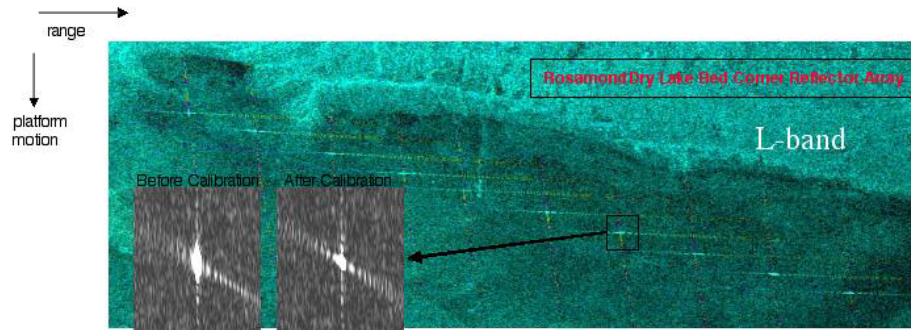


Figure 9: Example ATI L-band interferogram from Rosamond calibration site. The returns from the corner reflector array are evident across this scene. The effect of improving the common range delay calibration parameter is shown in the inset boxes. The interferometric phase is given by the color. The approximately uniform color of this scene means that it isn't moving, that it's relatively flat (no topographic phase) and that the antenna lever arm vectors are at least approximately correct.

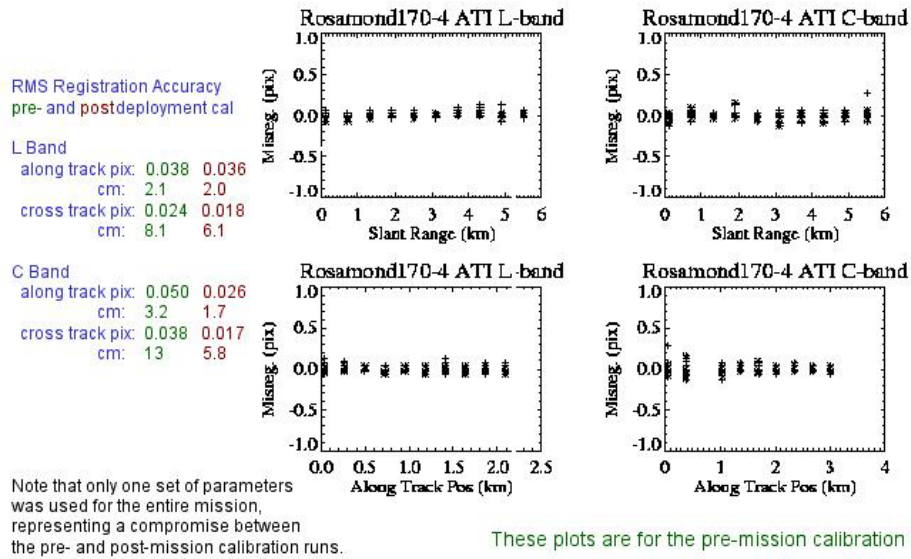


Figure 10: Co-registration of the PacRim 2000 data set over the Rosamond AIRSAR calibration site. The offset between the two interferometric channels is everywhere better than 1/20'th of a pixel. Only one set of calibration parameters is used for the entire three-month mission, and were a compromise between the parameters determined by the pre- and post-mission calibration data sets.

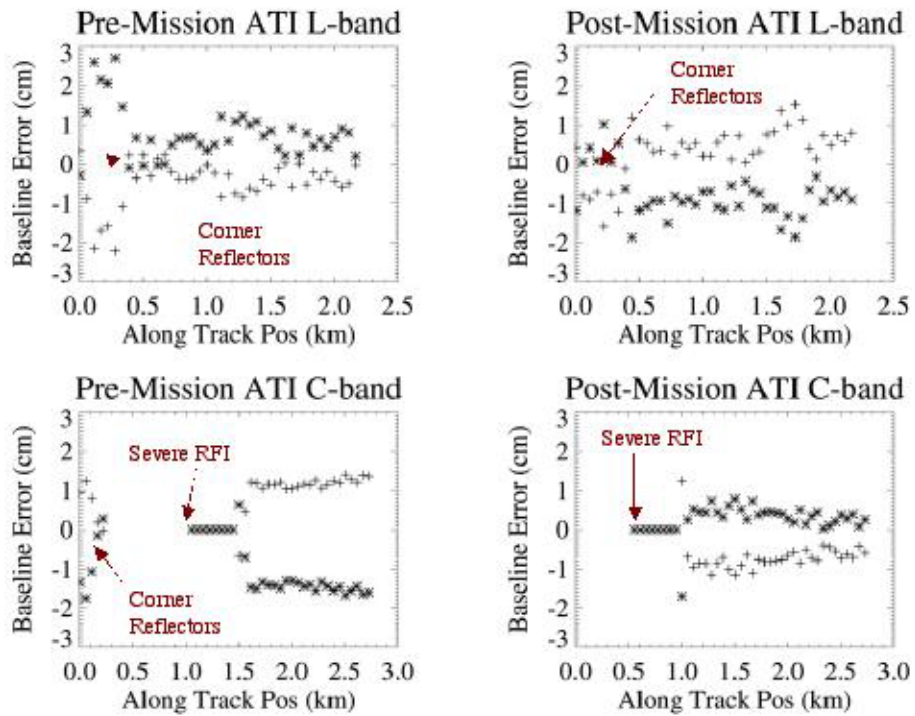


Figure 11: The baseline calibration for the PacRim 2000 ATI data. The calibration job is complicated by the corner reflectors (whose high contrast actually interferes with the baseline calibration) and some signal interference at C-band. The fit to the antenna lever arms was a compromise between the best pre-mission and best post-mission fits. There is about a half-centimeter error between the best fits, both in vertical and horizontal position of the lever arms, and the compromise calibration parameters.

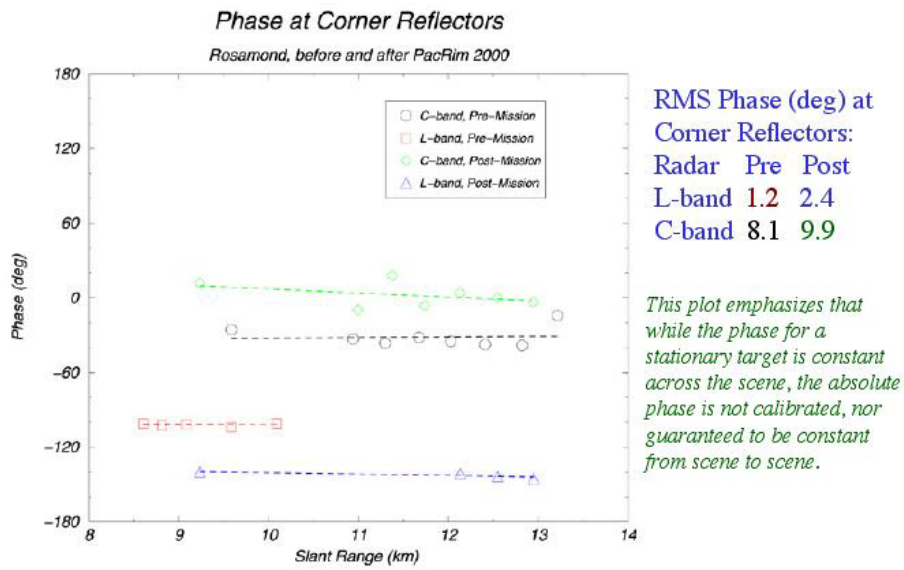


Figure 12: Relative phase calibration at the Rosamond dry lake bed. The (minimal) phase variation across this flat scene shows that the antenna lever arms are determined accurately. If the scene were perfectly flat (it almost is), nothing was moving in the scene (it was not) and the lever arms were correct, then there should be no systematic phase variation across the scene. The absolute phase has not yet been calibrated.

## 4 ATI Data Sets

Here we present the history of AIRSAR ATI data collection, as well as some of the data sets used to validate the AIRSAR ATI processor and evaluate its measurement accuracy.

### 4.1 Early AIRSAR ATI Data

ATI data has been collected by the AIRSAR system as far back as the late 1980's. However, this early data suffered from inaccurate motion measurement systems and early algorithms which performed little or no motion compensation. The end result was that early data sets had to be substantially “post-processed” to remove significant artifacts; i.e., a cross-track phase-ramp, which varied along-track was typically removed from the data before it could be interpreted as current measurements. In the present AIRSAR ATI processor, some of these motion artifacts can still be seen, but they are greatly reduced in magnitude; no “post-processing” of AIRSAR ATI data sets is currently performed to eliminate such artifacts.

Data acquired (whether ATI Data or of any other kind) prior to 1993 which have not already been processed cannot now be processed—the old technology tape readers have all failed beyond our ability (and funding) to have them repaired, and the tapes themselves have degraded beyond retrieval. Many, or most, of the standard POLSAR data sets from before 1993 were processed and archived to optical disk, and more recently, CD-ROM. But the early ATI processor was never part of the AIRSAR delivery system, so that none of any of the early data sets were archived.

Data collected during 1993 and 1994 can still be retrieved, but has not yet been processed for two reasons:

1. The motion measurement system was upgraded substantially (to an integrated GPS and INU system) in 1995. With this upgraded motion measurement system, much more accurate platform motion is recorded in the telemetry, allowing for better ATI data processing. The internal telemetry formats were modified significantly in 1995 to accommodate the new system. The current AIRSAR ATI processor was designed to take advantage of this improved measurement system, but is not currently compatible with the old telemetry format.
2. Around 1994–1995, the supercomputer on which the old ATI processor resided failed and could not be recovered. At that time, there was no ATI processing, nor anyone cognizant of the old ATI processor, at JPL, so ATI processing became unavailable for several years until the new processor (described here) was developed.

The ATI data collected during the 1993–1995 flight seasons is listed in Table 3.

1993 ATI Data		1994 ATI Data		1995 ATI Data	
Tape	Pass Name	Tape	Pass Name	Tape	Pass Name
93004	Golden-Gate251-1	94001	Golden-Gate45-1	95001	Rosamond170-4
93004	Golden-Gate45-1	94002	Golden-Gate45-1	95002	Golden-Gate320-3
93005	Golden-Gate180-1	94004	Rosamond170-5		
93005	Golden-Gate270-1	94008	Gulf-Mexico146-1		
93005	UC-Davis263-4	94009	Gulf-Mexico49-1		
93007	Rosamond170-3	94009	Gulf-Mexico30-1		
93010	Gulf-Mexico92-1	94010	Gulf-Stream230-1		
93010	Gulf-Mexico105-1	94010	Gulf-Stream140-1		
93010	Gulf-Mexico90-1	94038	Rosamond170-5		
93011	Gulf-Mexico180-1	94068	Gulf-Mexico59-1		
93011	Gulf-Mexico250-1	94068	Gulf-Mexico144-1		
93010	Gulf-Mexico360-1	94069	DuckPier62-1		
93012	Gulf-Rain185-1	94069	DuckPier332-1		
93030	CapeHatteras159-1	94069	DuckPier152-1		
93030	CapeHatteras180-1				
93030	CapeHatteras360-1				
93030	CapeHatteras270-1				
93030	CapeHatteras90-1				
93031	CapeHatteras270-2				
93033	Rosamond170-4				
93055	Rosamond170-5				

Table 3: ATI data collection from 1993 to 1995. In 1995, there was no ATI science data collection, only a single engineering checkout line and a single calibration line.

ATI Data Collection Site
South Pacific Ocean
South China Sea
Philippine Sea
New Zealand Transit
Kohala Coast (Four lines over ground truth)
East Australian Current (Four lines, one long transit)
East China Sea
Gulf of Thailand
Tasman Sea (Two lines)
Baringhead, New Zealand

Table 4: ATI data sets collected by AIRSAR during the 1996 Pacific Rim campaign.

## 4.2 The Pacific Rim 1996 Mission

In the 1996 PacRim campaign AIRSAR collected several ATI data sets during ocean transits between other data collection sites for the purpose of developing and validating an operational ATI processor. Table 4.2 lists these data sets.

Several data sets were collected at the Hawaii site, near the Kohala coast. We have not studied these data sets other than for the purpose of developing and validating the ATI processor, but there is clearly an interesting shear zone which can be seen in the correlation map (Figure 13) where the brightness of the pixel corresponds to the magnitude of the correlation (12). This shear zone is even more evident in the ATI phase (Figure 14) where the sharp discontinuity amounts to about 60 cm/s in velocity. Waves fields propagating across this scene are also in evidence. Also in evidence is the inadequate early calibration of the processor, which lead to substantial motion artifacts in the scene—showing as along-track phase variations. This data set was made publicly available<sup>2</sup> in December 2000 for investigators who wished to experiment with this mode of AIRSAR data. The data set includes imagery, interferograms and correlation maps for both L-band and C-band, providing these for both the “ping-pong” and “common-transmitter” baselines, enhancing the estimation of correlation times from the data.

## 4.3 EOCAP 1998

In Fall 1998 AIRSAR conducted the EOCAP data collection which included, in addition to the usual engineering checkout lines over San Francisco Bay and calibration lines over Rosamond Dry Lakebed, an experimental ATI collection for one investigator in the Gulf of Mexico (Figure 15) looking at a mesoscale eddy, and an ATI calibration/validation experiment over Monterey Bay.

For the 1998 data collection campaign only, the AIRSAR C-band radar was in the polarimetric interferometry configuration: the usual TOPSAR antennas

<sup>2</sup>See [http://airsar.jpl.nasa.gov/news/news\\_archive.htm#p4](http://airsar.jpl.nasa.gov/news/news_archive.htm#p4)

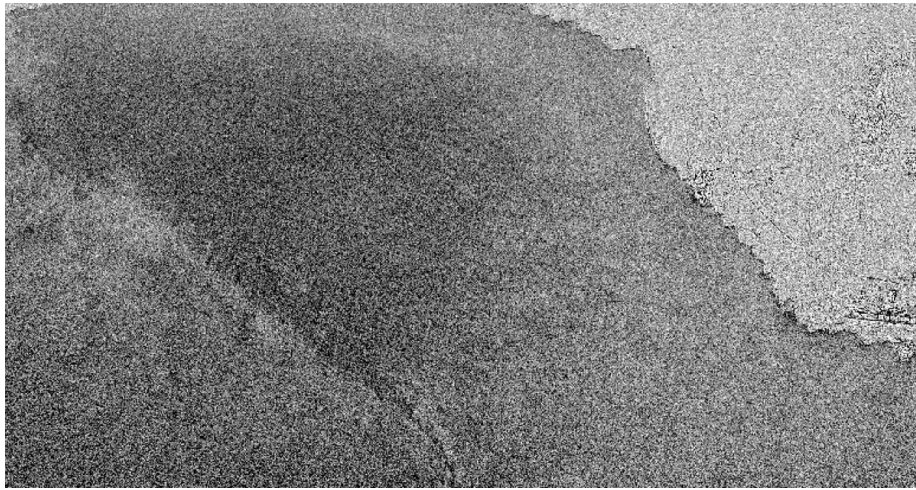


Figure 13: Interferometric correlation off the Hawaii Kohala Coast. The brightness of each pixel corresponds to the correlation magnitude: black is 0 (completely uncorrelated) and white is 1.0 (perfectly correlated). The upper right part of the image is the Island of Hawaii (the airport is at the far right just below the center of the scene) and a wind shear reflected on the surface of the ocean can be seen running from the lower middle of the image to the upper left. The platform was moving from right to left; near range is at the top of the image, far range at the bottom. See Figure 14 for the interferometric phase for this scene.

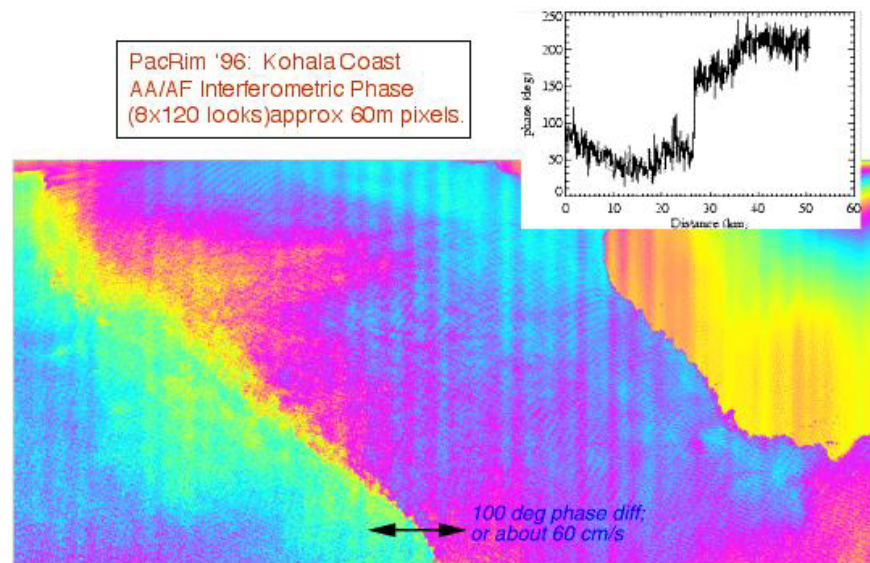


Figure 14: Along-track interferometric phase off the Hawaii Kohala Coast showing a shear zone. The image also shows the less accurate early motion-compensation for this data set. (Vertical bars) The platform was moving from right to left; near range is at the top of the image, far range at the bottom. The color is proportional to the interferometric phase difference. The inset shows the phase step across the shear zone.

were replaced with dual-pol antennas and an extra set of fast diode switches was introduced to switch the transmitted signal to the appropriate antennas, as well as switch the received signal to one of two C-band receivers. This had the advantage that we were able to acquire one polarimetric interferometry data set. Polarimetric along-track interferometry may be useful<sup>3</sup> for examining breaking wave events. It had, however, the disadvantage that fast high-power switch network was lossy and the antennas had a substantially worse gain. Thus, the C-band data from the 1998 data collection campaign are somewhat degraded compared to other campaigns.

### 4.3.1 Monterey Bay

The data collection plan for the Monterey Bay ATI Experiment is shown in Figure 16. Unfortunately for the cal/val experiment, which was conducted with several other participating ground-based radars, the winds were very low during the data collection. This means that the radar scattering cross-section was very low. Nevertheless, the ATI data do show a good ocean wave field (Figure 17) in both C-band and L-band data sets. These data also show that there were still uncorrected calibration errors: platform motion effects are in evidence (Figure 18) as vertical bars of phase along lines of constant position along-track. The interferometric correlation in these scenes is a function not only of the signal-to-noise, but also of how much temporal decorrelation there is during the time that the synthetic aperture is acquired. In particular, the waves breaking on the coast are quite bright at radar wavelengths, but are decorrelated due to the rapid changes in scatterer orientation within each pixel. This effect can be used to map out the surf zones, as shown in Figure 19.

The temporal decorrelation of the surf zones can be lessened, at the expense of azimuth resolution, by decreasing the time used to form the synthetic aperture. By reducing this time by a factor of about 10, the images shown in Figure 20 were obtained for this same Monterey Bay data line. Not only do the breaking waves show good correlation, but traffic moving along the Pacific Coast Highway can be seen.

---

<sup>3</sup>Personal communication with Brian Pollard, who presented initial results using this data at the PIERS2000 conference in Boston.

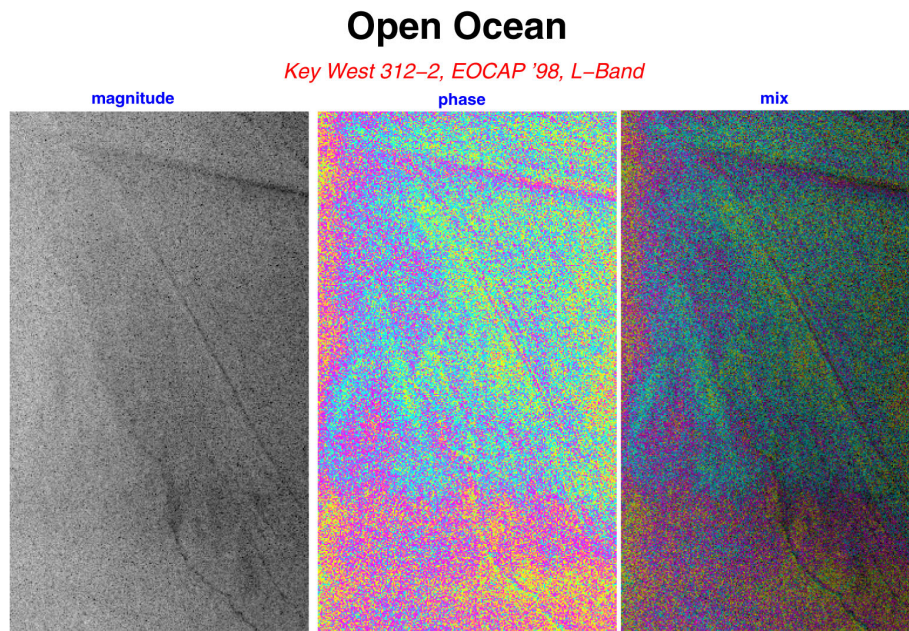


Figure 15: Segment of ATI data collected during the 1998 EOCAP data collection campaign over the open ocean near Key West. On the left is the SAR magnitude image, in the middle is the along-track interferometric phase interpreted as color (360 degrees of phase for a full color wrap) and on the right is a mix of these two, where the brightness is given by magnitude and color by phase.

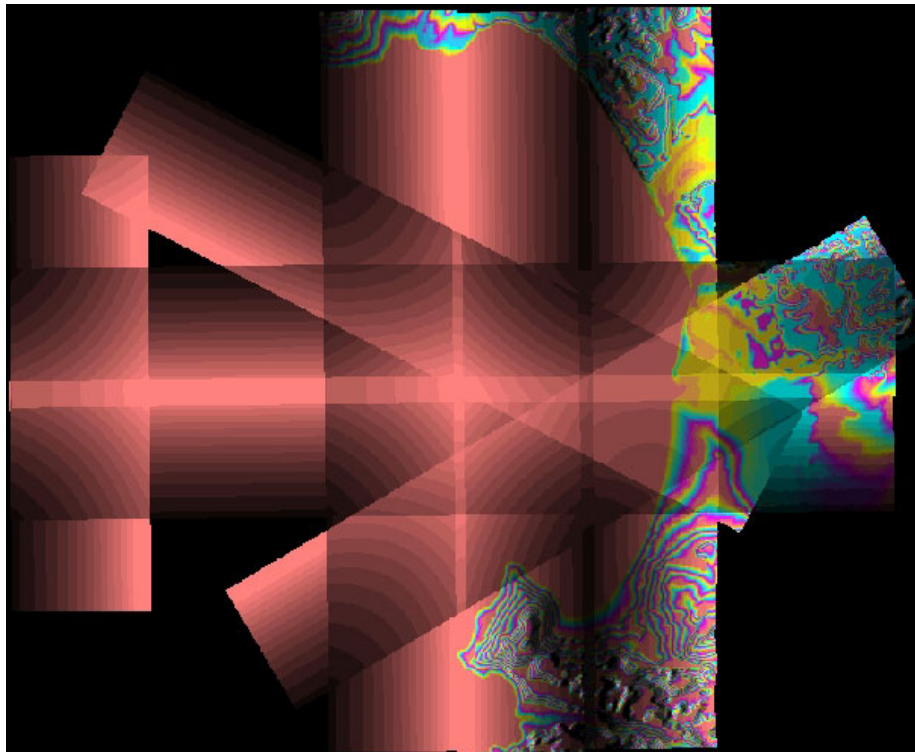


Figure 16: Plan of ATI data collection for the Monterey Bay Experiment. These flight lines were collected. However, due to low winds on the day of collection, the data are expected to be less useful than hoped. Only one of these lines has been processed so far, and is shown in Figures 17 and 18.

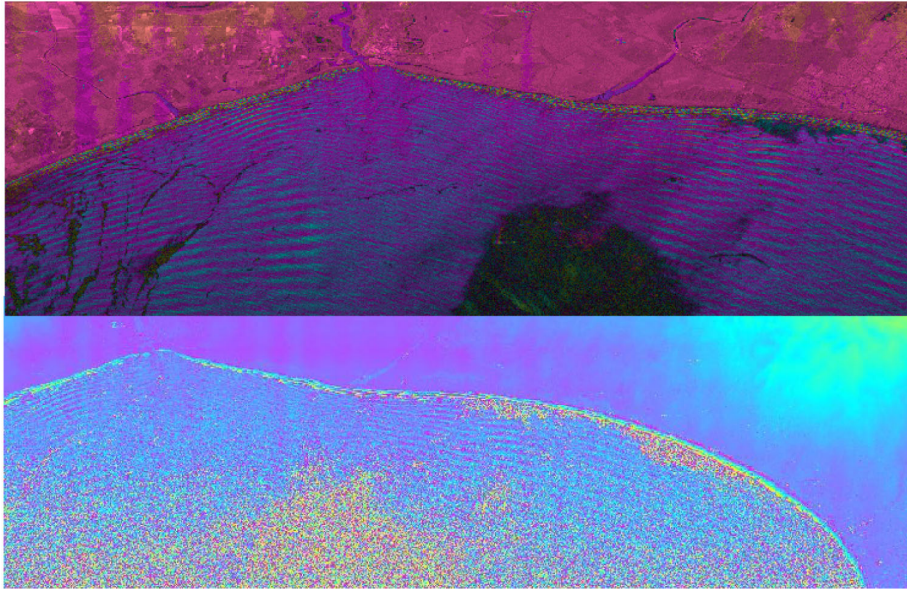


Figure 17: Pair of along-track interferograms. The upper interferogram was acquired with the L-band system. The image is modulated by the radar brightness, while the color corresponds to the interferometric phase difference. The lower image is for C-band, acquired at the same time as the upper image. Only the phase is shown in the lower image. The dark area shows significant decorrelation in the C-band interferogram. During this deployment, AIRSAR was configured with the experimental (and lower gain) POLTOP antennas and lossy switch network at C-band, so that the signal-to-noise was as much as 9 dB worse in one of the C-band channels. Nevertheless, two or three separate wave trains can be seen in these data propagating into the shore and reflecting off of it.

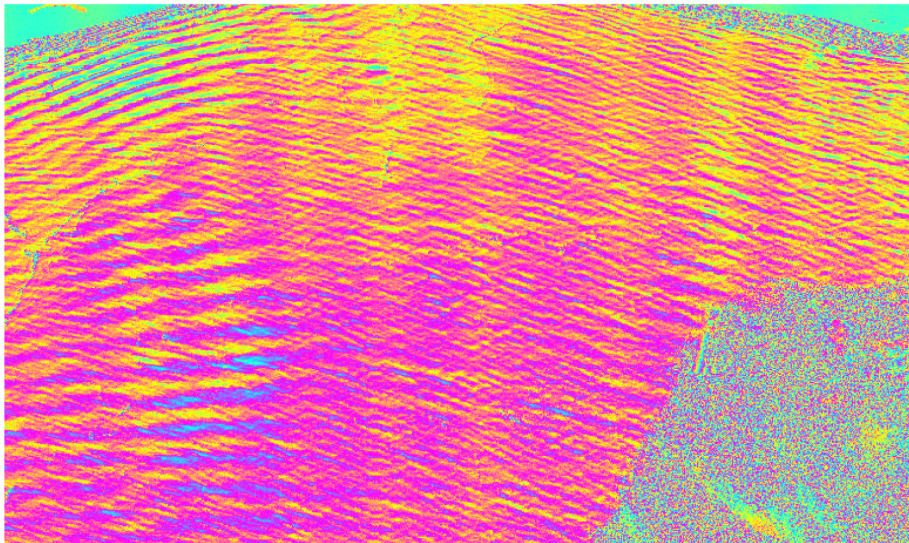
*EOCAP '98: L-Band AF/AA, 4x24 looks, 180 degrees color wrap*

Figure 18: Detail of the phase of L-band interferogram shown in Figure 17. Here the color table has been altered so that a full color-cycle is accomplished by only 180 degrees of phase. This highlights the separate wave trains in the scene, but also the motion artifacts which are evident as the vertical bars of phase. (The platform is moving from right to left, and the near-range is at the top of the scene.) The coastline is at the top of this scene, and the dark area is at the lower right, showing significant decorrelation due to lower SNR.

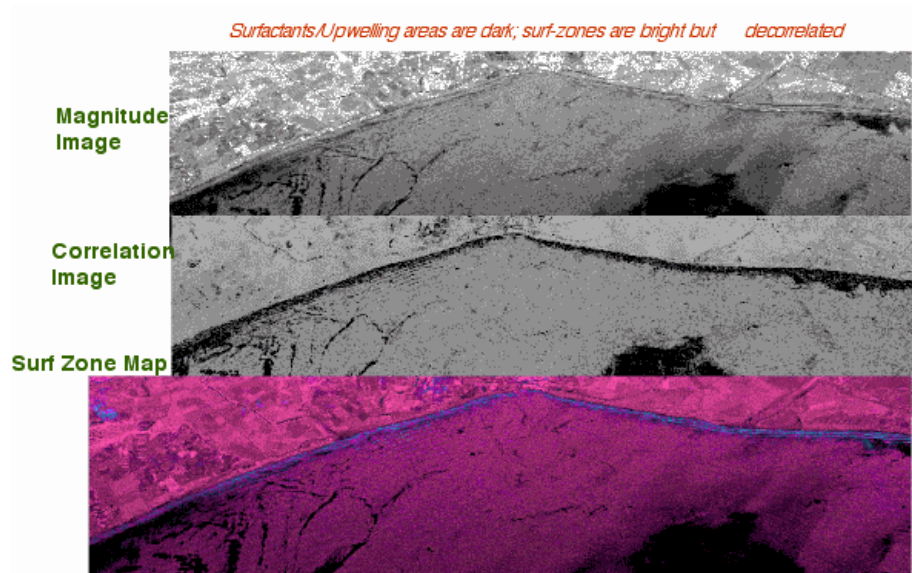


Figure 19: Mapping the surf zone at Monterey Bay. The upper image is the radar brightness—the breaking waves have a fairly bright cross-section compared to the rest of the ocean. Meanwhile, in the middle image, the interferometric correlation magnitude shows that both the low signal to noise areas (areas dark in the top image) as well as the fast-moving breakers along the coast, are quite decorrelated. This combination can be used (bottom image) to highlight areas which are decorrelated, but not due to low SNR. The blue area all along the coast is the “surf zone” where the waves are breaking.

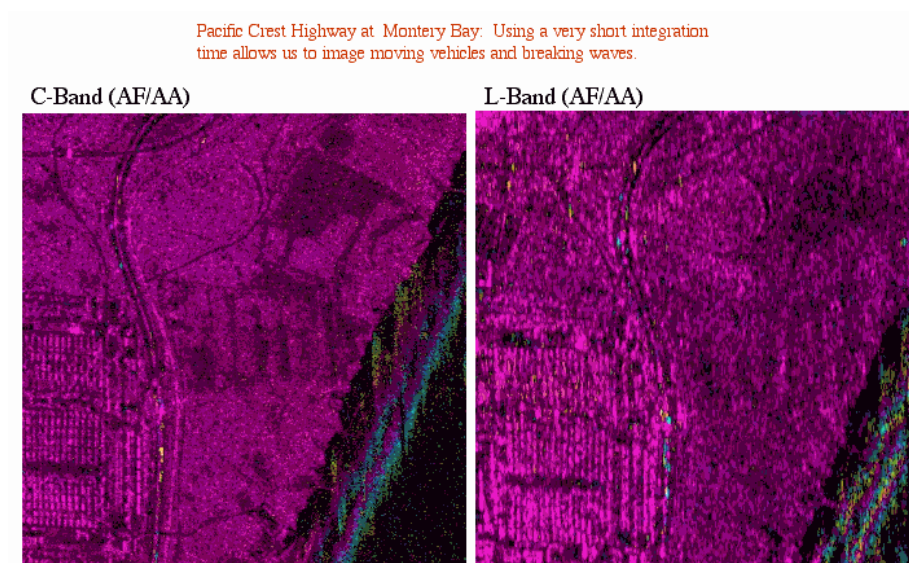


Figure 20: C-band (left) and L-band (right) interferograms reprocessed from the same Monterey Bay data line shown in the previous figures, but with about a factor of 10 reduction in the time used to form the synthetic aperture. The breaking waves coming into the coast from the lower right are now coherent. Traffic can be seen moving along the Pacific Coast Highway. Note that the C-band and L-band data are acquired at slightly different squint angles, so that the vehicles will not be imaged at the same place by the two radars unless special provision is made to fix the processing squint of both radars to the same value.

### 4.3.2 San Francisco Bay

We also collected data over one of our standard engineering checkout sites, San Francisco Bay. The correlation time in the bay is somewhat longer than in the open ocean, and the swift currents through the bay are in evidence (Figure 21), as well as the wave field (Figure 22) diffracting off of Point Bonita. We used this site to investigate acquiring data at different baselines ( $\Delta t$ ): as expected the longer baseline shows more velocity sensitivity. (See the comparison showed earlier in this paper, Figure 7.

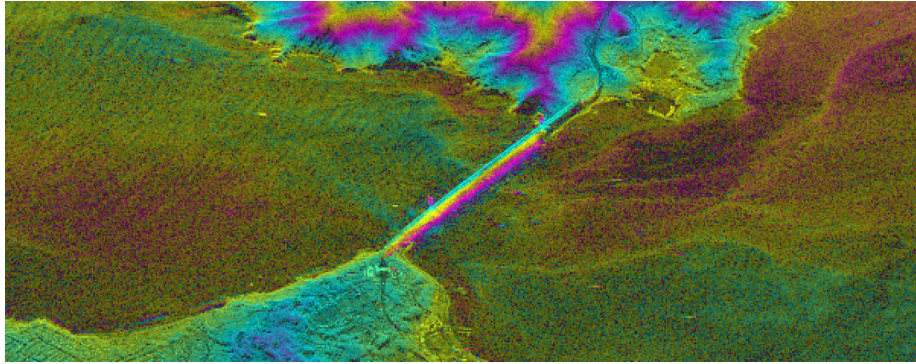


Figure 21: Engineering checkout data acquired over the Golden Gate Bridge and San Francisco Bay in 1998. Only C-band data were acquired at that time, as we did not yet have permission to radiate at L-band for that season. (Permission was granted starting with the next flight.) This is a “ping-pong” interferogram, where first the forward antenna is used both to transmit and receive, followed by the aft antenna, used both to transmit and receive. The topographic phase discussed at the beginning of this paper is in evidence over the land, but so are the swift currents flowing along the Bay. The swell can be seen propagating from left to right in this image from the open ocean into the bay. Figure 22 highlights this part of the interferogram.

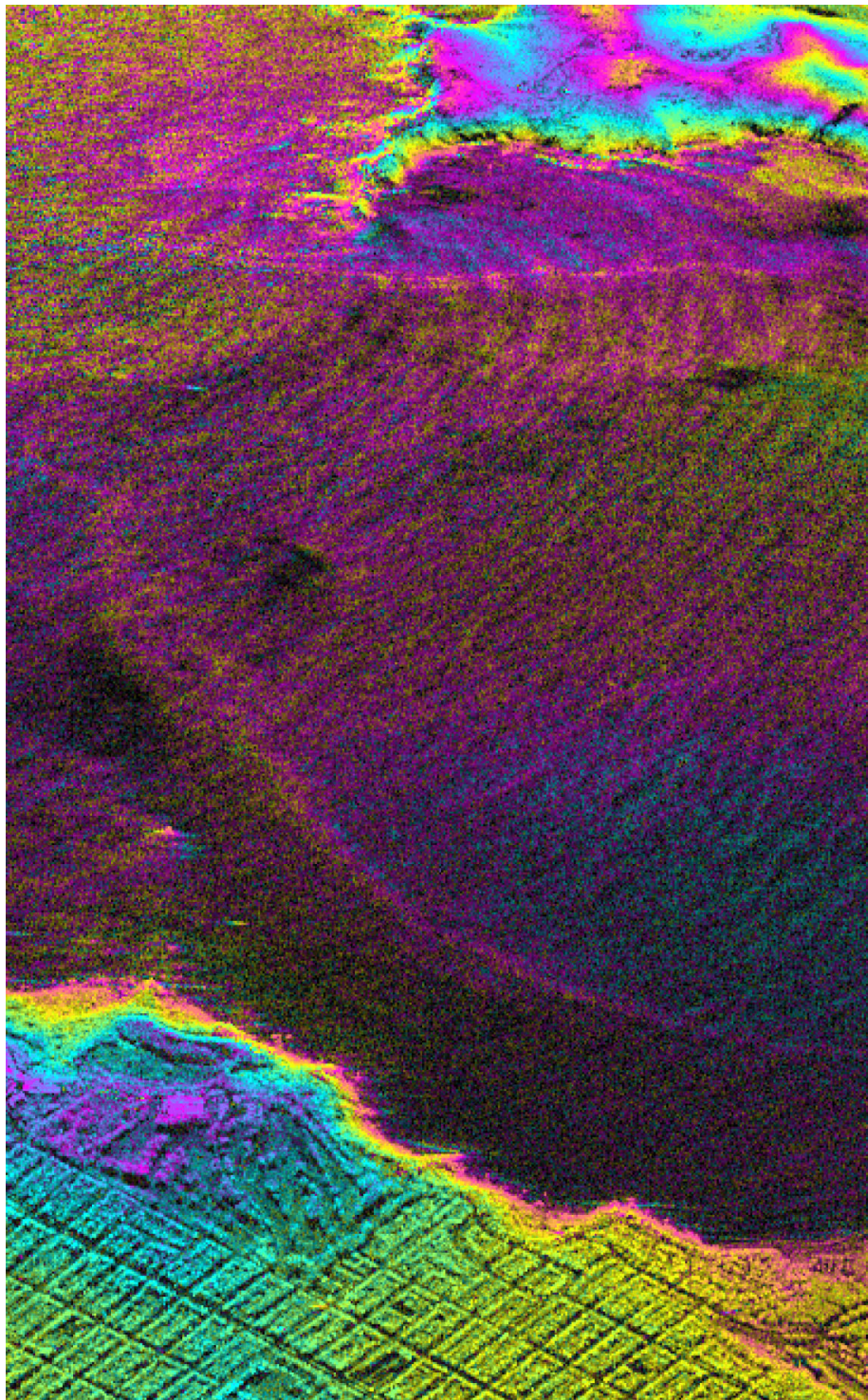


Figure 22: Detail of Figure 21 showing the Bay and the part of San Francisco across from Pt. Bonita where the swell is entering the bay and diffracting off of Pt. Bonita.

#### 4.4 AirSci 1999

Besides the usual engineering checkout flights and the calibration flights, only one ATI data set was collected in 1999: the Straits of Juan de Fuca in the Pacific Northwest. Nevertheless, this proved to be an interesting data set, where the tidal outflows from the bays into the straits were directly observed by the ATI system. The plan of this data line is shown in Figure 23. This data set has turned out to be of interest because it recorded a strong tidal current (Figure 24) in the Straits at the time the data were acquired. This has allowed comparison of the C-band and L-band radar measurements, which appear to be in good agreement on the estimates of the current velocity. (Figure 25).

Several interesting features are apparent in this data set, including a nicely meandering current boundary (Figure 26) and the eddies and tidal drag around the Smith Island National Wildlife Refuge, Figure 28. Finally, there are a few ships captured in this data set, Figure 27. These ships can be used to perform an independent verification of the ATI phases, and to remove the unknown absolute phase offset. This technique has been successfully demonstrated by Dukjin Kim, *et al.*, elsewhere<sup>4</sup> in these proceedings.

---

<sup>4</sup>Remote Sensing of Ocean Waves and Currents Using AIRSAR Along-Track Interferometry (ATI), by Duk-Jin Kim and Wooil M. Moon, (School of Earth and Environmental Science, Seoul National University), David A. Imel and Delwyn Moller, (JPL), *Proceedings of the 2002 AIRSAR Earth Science and Applications Workshop*, ed. by David A. Imel, 4–6 March 2002.

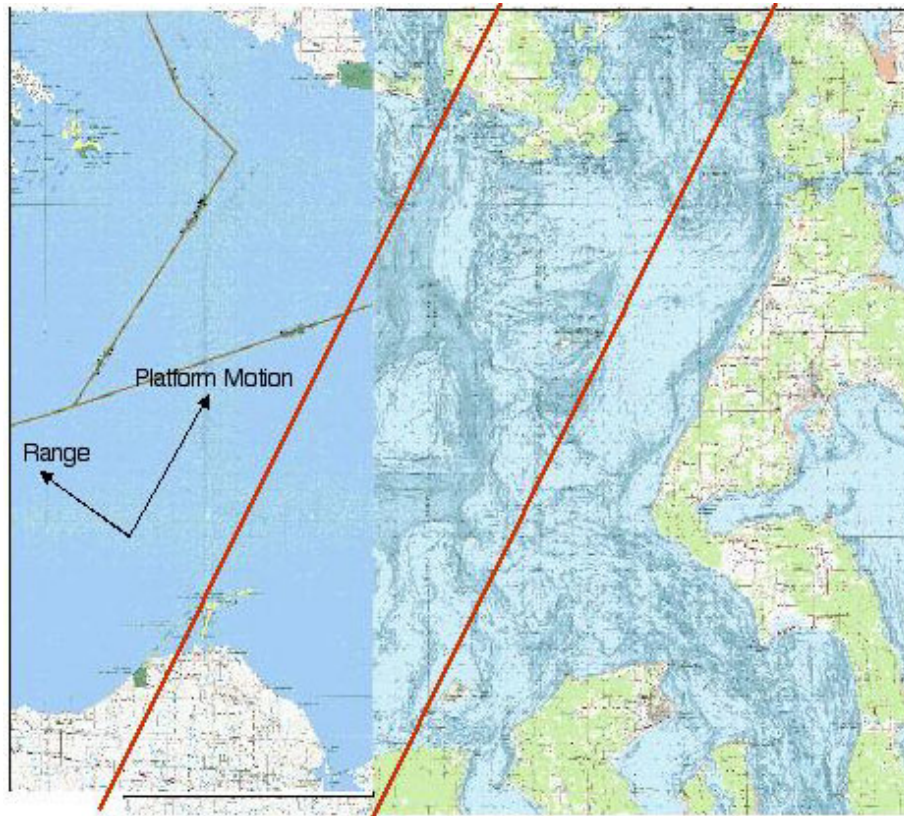


Figure 23: Plan of the data line acquired over the Straits of Juan de Fuca. The line has land at the beginning and end of the scene, which is convenient for calibration within the data set. It also crosses several ferry routes and Smith Island National Wildlife Refuge. The bays in the lower and upper right (East) of the scene empty into the Straits, leading to strong tidal inflows and outflows. The currents can reach 8 knots.

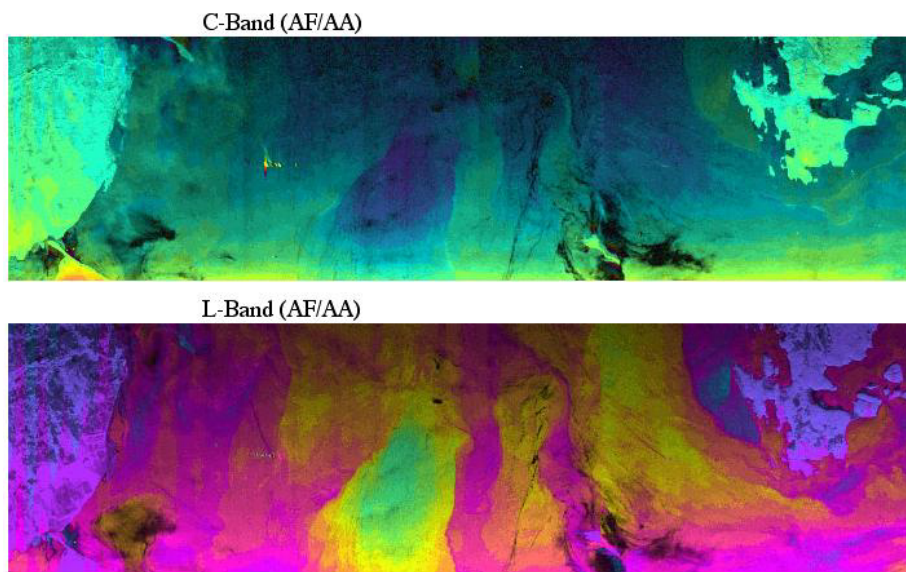


Figure 24: The interferograms acquired over the Straits of Juan de Fuca. The upper image is the C-band interferogram, and the lower, L-band. Both of these are “common-transmitter” mode interferograms, though the data were collected in “ping-ping” mode. Land is visible as the patches of approximately constant color (interferometric phase) at the beginning and end of the interferograms.

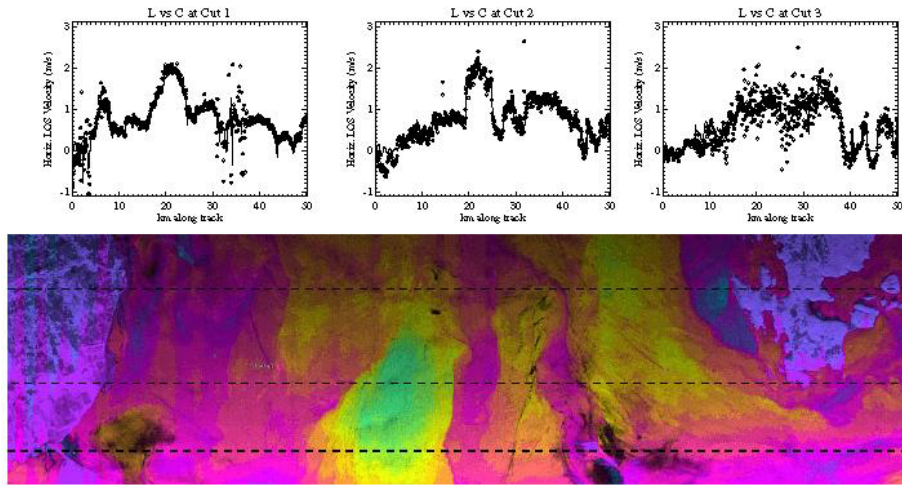


Figure 25: Comparison of L-band and C-band current values, where a phase offset given by the phase over land has been subtracted from each interferogram and the motion has been projected onto the horizontal. The resulting current measurements for L-band and C-band are in good agreement. The three plots above the L-band interferogram shown correspond to the cuts taken at three constant ranges (dashed lines) across the scene. The left-most plot is the nearest range, the right-most plot, far-range. In the image, near-range is at the bottom, and the platform is traveling from left to right. In the plots, the solid line is the L-band phase, while the scattered points are the C-band phases. Notice that where the image is darker, the C-band points are much more scattered: the signal-to-noise is worse and therefore the phase-noise increases. But in general, the current profiles measured by the two different radars track very well. The maximum current observed here corresponds to an outflow of about 4 knots.

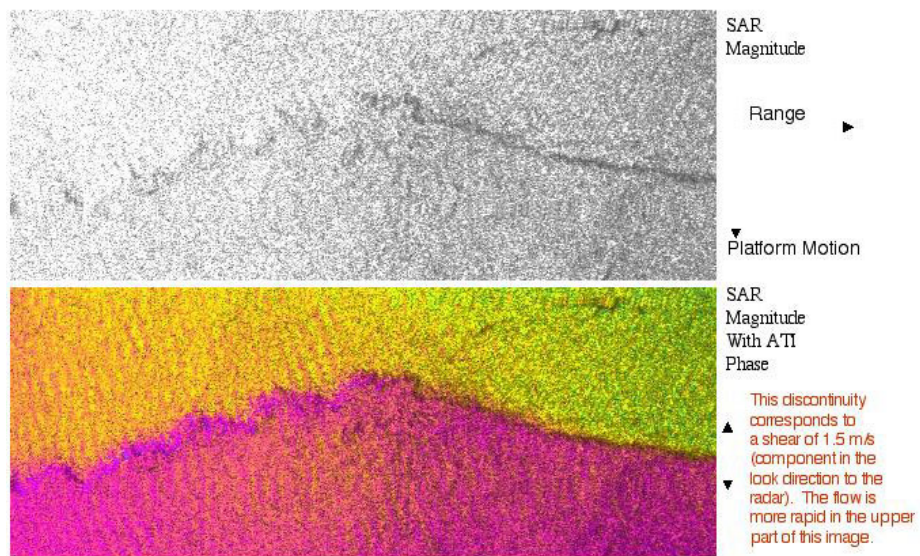


Figure 26: A current boundary in the data acquired over the Straits of Juan de Fuca. The waves propagating across the current boundary appear to be diffracted. Notice that while the boundary shows up in the SAR magnitude (upper) image as a region of upwelling and therefore smoother, darker surface, the current difference on either side of this boundary is much more obvious in the interferogram than in the SAR magnitude image alone.

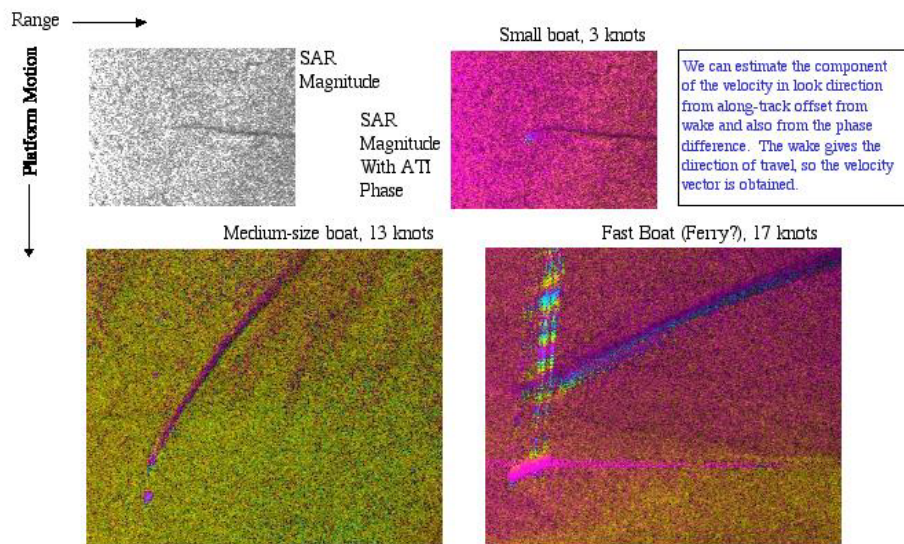


Figure 27: Ships observed in the Straits of Juan de Fuca along-track interferogram. The displacement of the ship from the wake gives an independent estimate of the ship's motion along the line-of-sight to the radar, and the wake gives the direction of motion. Thus, ships can be used as an independent self-calibration of an ATI data set. Note also that the ship itself is much easier to detect in the along-track interferogram than in the SAR magnitude image alone.

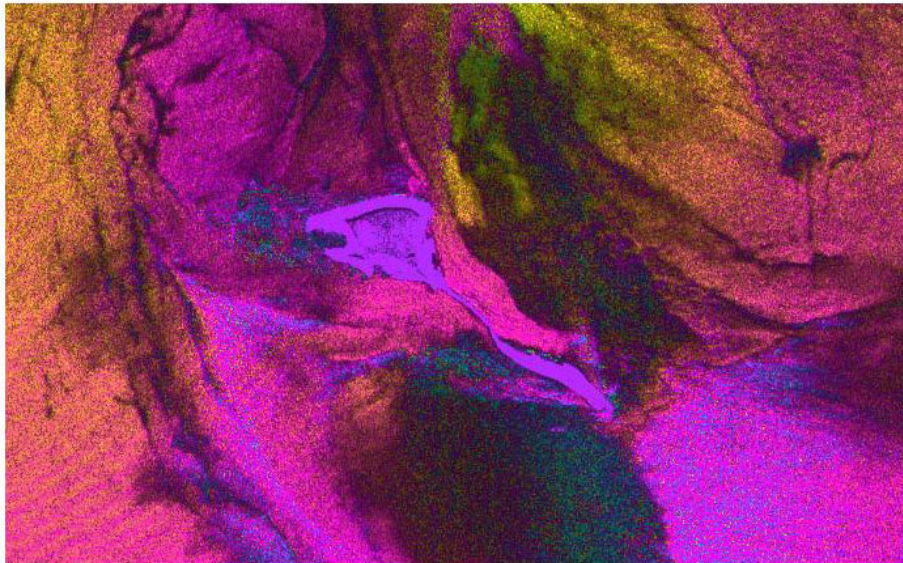


Figure 28: Eddies in the tidal flow around Smith Island National Wildlife Refuge.

## 4.5 PacRim 2000

A significant quantity of ATI data was collected during PacRim 2000, since the ATI processor was now available at the beginning of this mission. Tables 5–10 list the sites where ATI data were acquired, and Figures 29 and 30 depict some of the ATI data products which have already been processed and delivered. All told, 49 ATI flight lines were acquired over 26 different sites for a total collection of about 42000 km<sup>2</sup>. For PacRim 2000, ATI data were acquired in two different modes:

**ATI2** This was the “standard” ATI collection mode, where both C-band and L-band radars collected ATI data in common-transmitter (CT) mode, as opposed to ping-pong (PP) mode. CT mode ATI data have better SNR, since more pulses are used to form the synthetic aperture (i.e., more looks) and the losses to the are much larger at L-band as the signal propagates 20 meters down the aircraft fuselage to the forward antenna. Since we only transmit from the aft L-band antenna in CT mode, we avoid half of those extra losses.

**SATI** In SATI mode, C-band data are collected in POLSAR mode, while the L-band data are collected in ATI mode. None of these data have been processed yet, but in principle, the processing should be the same, except that the ATI data and the POLSAR data will not be delivered as co-registered data products.

At the end of 2001, the ATI processor was upgraded with a geo-location algorithm: using local sea-level as the elevation reference, products are now generated which are geo-located in the SCH coordinate system. (See the Data Product documentation on the AIRSAR web-site for a description of this coordinate system.) These new products specify each pixel in the SCH coordinate system, whose transformation to the WGS-84 coordinate system (via a peg-point and heading) is well-defined. An example of such a data product is shown in Figure 31. Since the data are now geo-located, the C-band and L-band along-track interferograms may now be co-registered, allowing for more direct multi-frequency ATI data analysis.

Tape	Flight Line	Notes
00001	goldengate360-3	ATI2 Engineering checkout
00001	goldenGate180-4	SATI Engineering checkout
00002	rosamond170-3	Pre-mission calibration
00002	rosamond170-4	Pre-mission SATI calibration
00003	vandenburg270-1	Ocean calibration
00005	rosamond170-4	Pre-mission calibration backup
00005	rosamond350-5	Pre-mission calibration
00005	rosamond350-6	Pre-mission calibration backup
00105	rosamond170-4	Post-mission calibration

Table 5: PacRim 2000 engineering checkout and calibration data lines. Except where noted, all lines were flown in the ATI2 mode.

Tape	Flight Line	Notes
00025	macquarieisland193-2	
00035	lizardisland140-1	
00038	palmislands65-1	
00038	ribreef245-1	
00040	daintree180-2	
00051	darwinharbour319-1	

Table 6: PacRim 2000 ATI lines acquired over Australia. (The ribreef line is over the Great Barrier Reef.)

Tape	Flight Line	Notes
00053	kinabalu210-1	SATI
00055	palauredang270-1	
00055	palauredang90-1	SATI
00055	pekan180-1	
00056	trengganu131-1	SATI

Table 7: PacRim 2000 ATI lines acquired over Malaysia. SATI lines are noted.

Tape	Flight Line	Notes
00076	muroran226-1	processed 21 May 2001
00077	izu,japan84-1	processed 20 May 2001
00077	kumanonada214-1	
00079	fukuoka,japan129-1	processed 26 May 2001
00080	kuroshio,japan150-1	processed 12 Jul 2001
00080	yakushima146-1	processed 31 May 2001
00080	yakushima205-1	

Table 8: PacRim 2000 ATI lines acquired over Japan. The one-year PI exclusive-use period ends one year after the processing date listed.

Tape	Flight Line	Notes
00091	barberspoint90-9	
00091	barberspoint90-10	
00091	barberspoint90-11	
00091	barberspoint270-9	
00091	barberspoint270-11	
00091	barberspoint270-13	
00091	kahoolawe72-1	
00092	kahoolawe72-1	
00093	barberspoint90-9	
00093	barberspoint90-10	
00093	barberspoint270-9	
00093	barberspoint270-10	
00094	kahoolawe72-1	

Table 9: PacRim 2000 ATI lines acquired over the Hawaiian Islands. Barber's point is on the Island of Oahu.

Tape	Flight Line	Status
00008	equatorcrossing207-1	
00009	makatea51-1	
00015	tubai344-1	
00022	whiteisland,newze0-1	
00064	lingayengulf102-1	
00064	lingayengulf339-1	
00068	southtaiwan321-1	processed 16 May 2001
00074	ulsan107-1	processed 04 April 2001
00074	ulsan197-1	

Table 10: Other PacRim 2000 ATI lines acquired over various sites, including the Equator, French Polynesia, New Zealand, the Philippines, Taiwan and South Korea. The one-year PI exclusive-use period ends one year after the processing date listed.

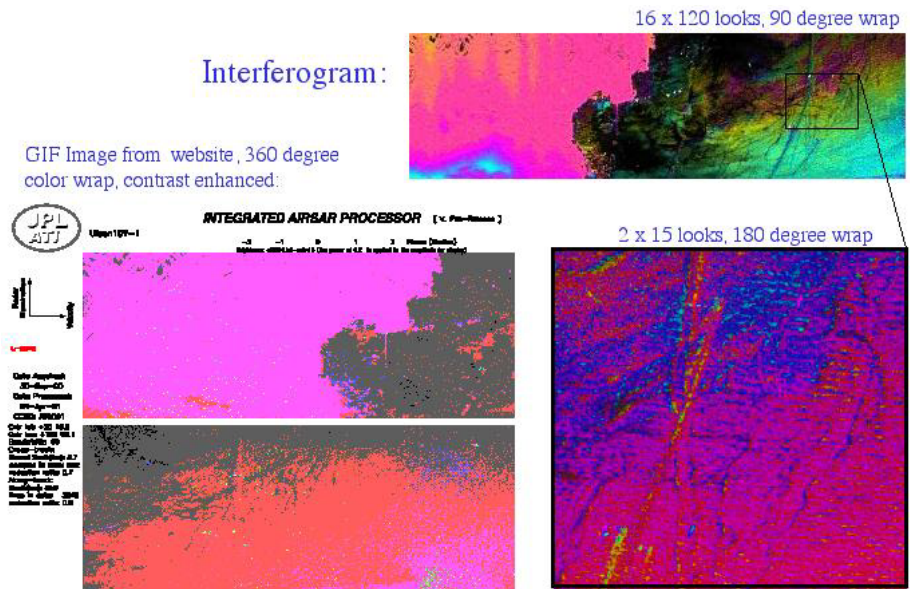


Figure 29: PacRim 2000 ATI data product from Ulsan, S. Korea.

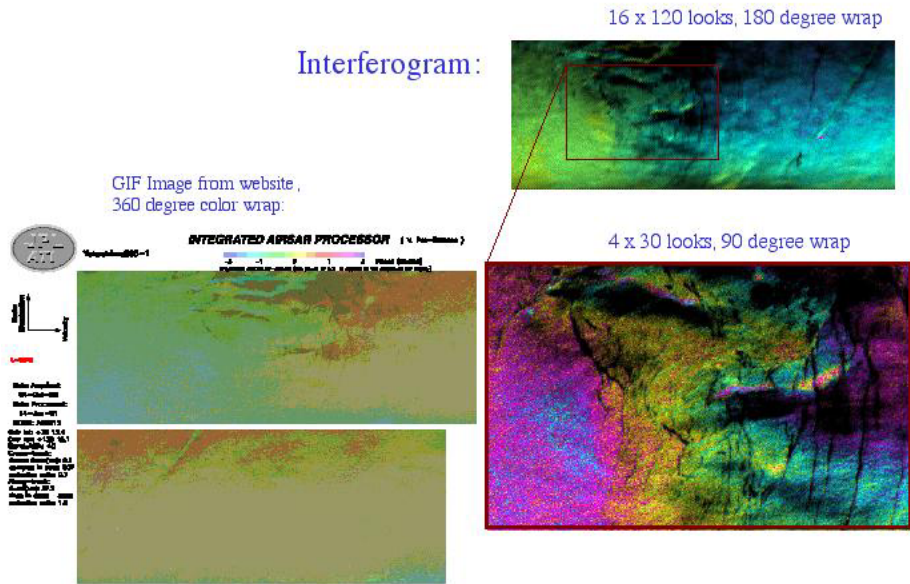


Figure 30: PacRim 2000 ATI data product for Yakushima, Japan.

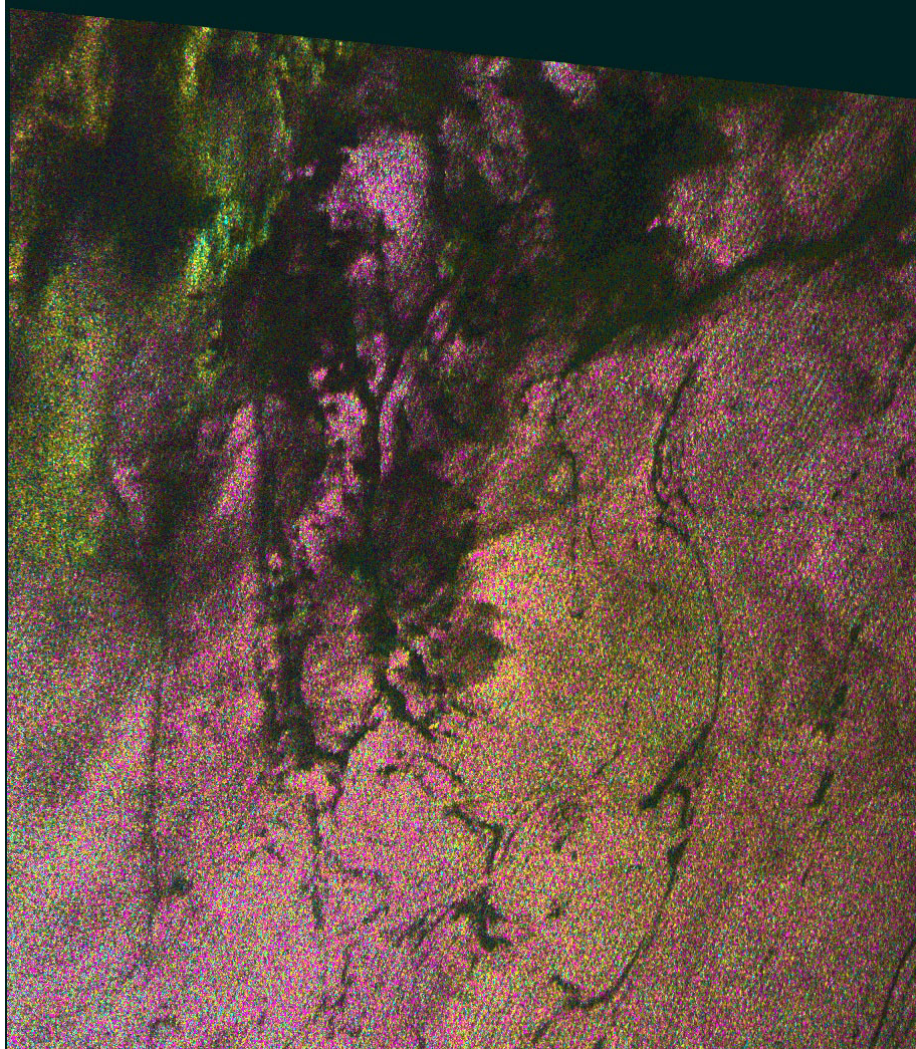


Figure 31: Part of a geo-coded L-band ATI velocity map acquired off the coast of Japan near the Kuroshio current. The post spacing of these data is 10 meters. Each pixel in this scene can be converted from its SCH-coordinate to a WGS-84 latitude, longitude and elevation. The color-wrap here corresponds to 4 m/s, and the brightness of the scene corresponds to the (uncalibrated) radar brightness.

## **4.6 IceSar 2002**

In addition to the usual engineering checkout ATI data lines over San Francisco Bay and the calibration lines over Rosamond, during IceSAR'02 AIRSAR will collect ATI data off the coast of Southern California to study eddies there and outflow from the rivers into the coastal oceans.

## 5 Performance

There are a couple of “internal” measures of the quality of the ATI data sets which can be made without reference to external ground (or sea) truth. One is the relative phase-noise of the scene, or equivalently, the relative velocity precision. Another statistic is the co-registration accuracy of the interferogram. We discuss the latter first.

### 5.1 Interferometric Alignment

As mentioned earlier, the L-band ATI antenna separation is 20 meters. This means that by the time the second antenna is imaging the scene at the same place as the first antenna, the aircraft platform has had the opportunity to undergo significant motion. A change of yaw of 0.1 degrees in that time period is a change in propagation distance corresponding to 55 degrees of interferometric phase, or 18 cm/s of velocity, if uncorrected. Therefore accurate calibration of the antenna lever arm vectors and application of motion-compensation and pulse-resampling algorithms is critical to the successful generation of an along-track interferogram. The AIRSAR ATI processor monitors the alignment of the two interferometric channels everywhere in the scene as a measure of the success of the calibration and motion-correction algorithms. An example of this alignment was shown in Figure 10 for calibration data acquired during PacRim 2000. Figure 32 shows what happens when there is excessive motion beyond what has been correctly compensated. By contrast, the PacRim 2000 have all shown good motion alignment thus far. See, for example, Figures 33 and 34.

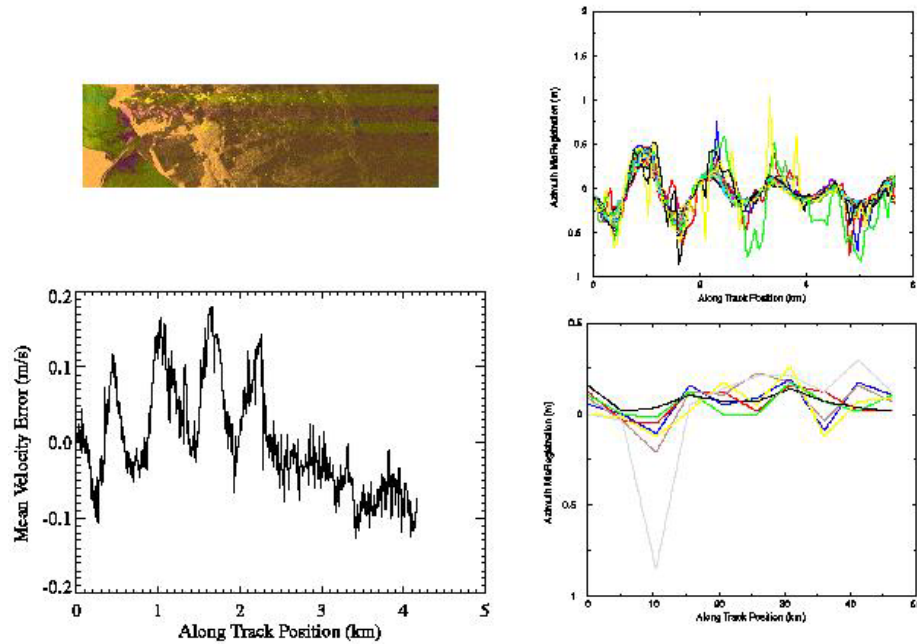


Figure 32: The effect of motion errors on the current velocity measurement for the Straits of Juan de Fuca data set. Here, the beginning of the data line, which is over (stationary) land is examined. The interferogram extract (upper left) shows clear motion-related artifacts: the platform is moving from top to bottom in this image. The right side plots show the azimuth mis-registration in meters. The different colored curves on this graph represent the azimuth mis-registration estimated at different ranges: from near range (black) to far range (grey). The plane has substantial residual platform motion at the beginning of the line, and the motion compensation is not perfect. Therefore an azimuth misregistration of about 1 meter peak-to-peak occurs, corresponding to velocity errors of not quite 20 cm/s. However, these systematic errors soon decrease substantially as the platform motion settles down. By the time data is being acquired in the straits, the rms velocity error is closer to 3 cm/s.

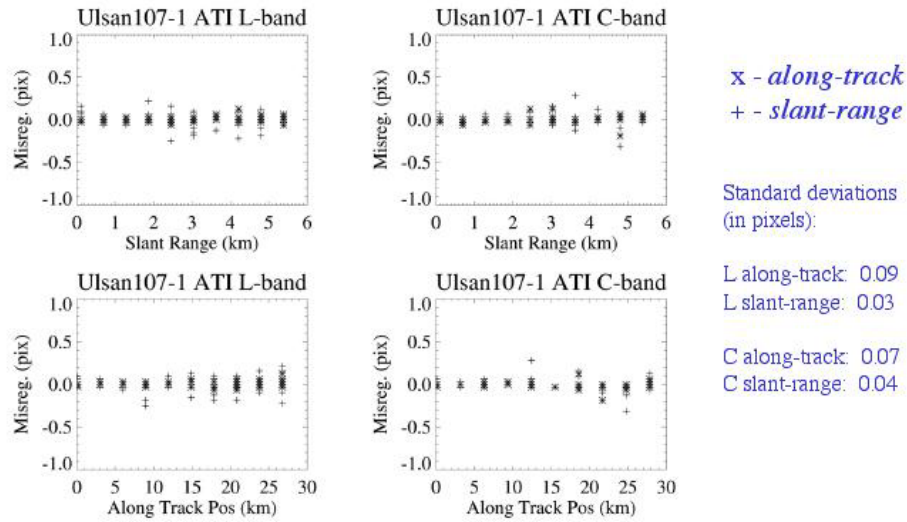


Figure 33: Graphs of motion alignment for the Ulsan107-1, South Korea ATI data line. The co-registration is better than 0.1 pixels (in the single-look complex slant-range interferogram) both in range and azimuth, and for both L-band and C-band interferograms. The upper graphs plot the co-registration as a function of slant-range, where several points are plotted for each range, corresponding to different along-track estimates. Similarly, in the lower plots the co-registration is plotted as a function of along-track position, and each position has several points plotted for the estimates made at different ranges.

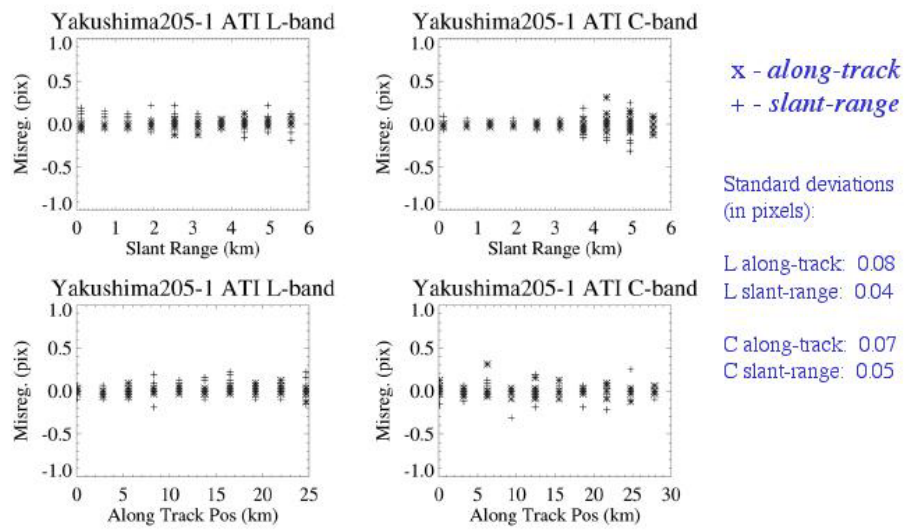


Figure 34: Motion alignment graphs for the Yakushima205-1, Japan ATI data line. See Figure 33 for description of the graphs. Here again the alignment is better than 0.1 pixels (in the single-look complex slant-range interferogram) both in range and azimuth and for both L-band and C-band.

## 5.2 Phase Noise

The phase accuracy of an ATI product is related to the signal-to-noise ratio (SNR) through the interferometric correlation:

$$\gamma_n = \frac{1}{1 + \text{SNR}^{-1}} \quad (19)$$

and

$$\gamma = \gamma_n \gamma_t \quad (20)$$

where  $\gamma_t$  is the temporal decorrelation of the scene, and is actually a quantity of physical interest, as mentioned in section 1.1:

$$\gamma_t = e^{-t^2/\tau_c^2} \quad (21)$$

where  $\tau_c$  is the coherence time (Figures 35 and 36) for the scattering scene. (Note that some authors use  $\tau'_c = \tau_c/\sqrt{2}$ .)

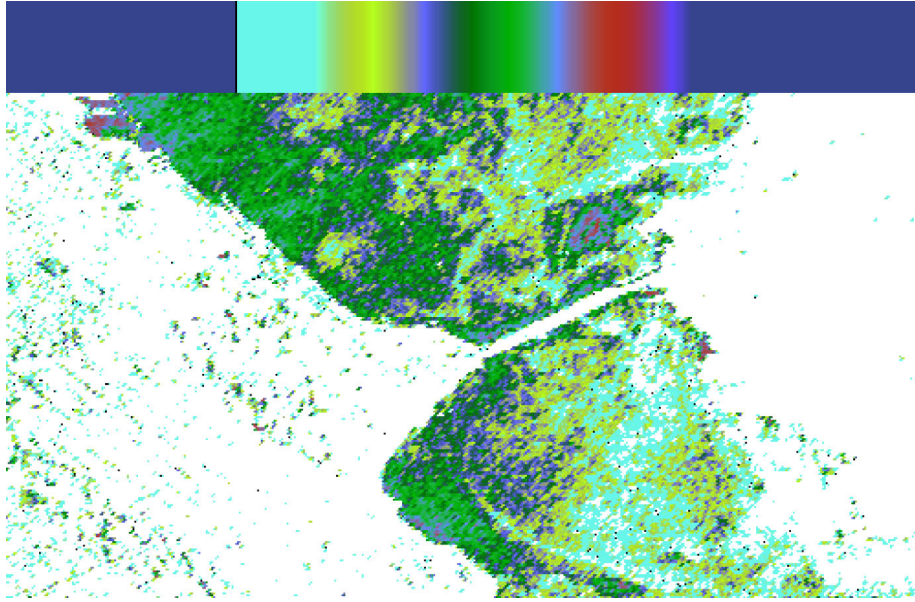


Figure 35: Coherence time estimated for a C-band correlation map over the Golden Gate Bridge in San Francisco, CA. The color bar above shows the scale from white (infinite coherence time) to dark blue (no coherence). A histogram of these values is shown in Figure 36.

The correlation then determines the root-mean squared phase noise:

$$\sigma_\phi = \frac{1}{\sqrt{2N}} \frac{\sqrt{1-\gamma^2}}{\gamma} \quad (22)$$

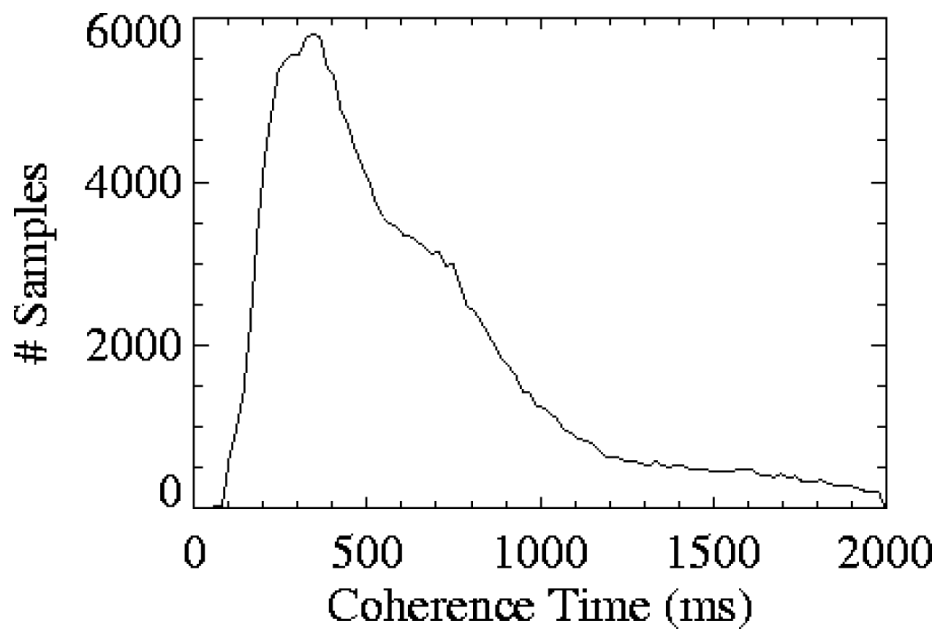


Figure 36: Histogram of coherence times for the image shown in Figure 35. The long tail corresponds to land coherence. The peak coherence time in the Bay seems to be about 300 ms.

where  $N$  is the number of looks. The phase noise determines the minimum detectable velocity component, as well as the accuracy with which a velocity component can be measured:

$$\text{Velocity Component Uncertainty} = \frac{\lambda}{4\pi\Delta t}\sigma_\phi. \quad (23)$$

Alternately, the ambiguous velocities from Table 1 can be used to obtain the same quantity for each AIRSAR ATI mode:

$$\text{Velocity Component Uncertainty} = \frac{(\mathbf{n} \cdot \mathbf{u})_{\text{amb}}}{2\pi}\sigma_\phi. \quad (24)$$

Phase noise estimates for the Straits of Juan de Fuca data (Figure 37) and the PacRim 2000 data sets discussed in the previous section: Ulsan, South Korea and Yakushima, Japan (Figures 38 and 39) show that the AIRSAR instrument is sensitive to velocities as small as a few cm/s, depending on the spatial resolution, but that the velocity accuracy is significantly worse in the far-range for the lower-SNR C-band radar.

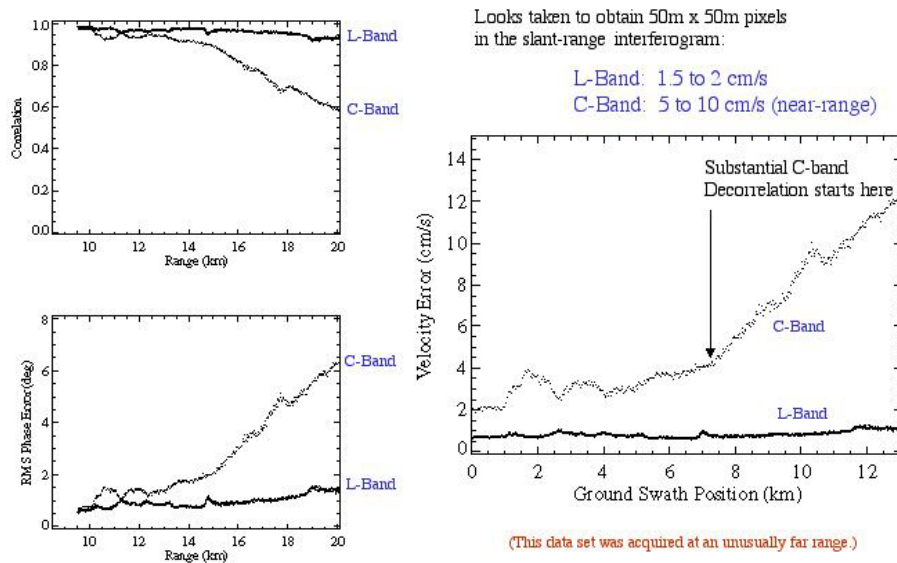


Figure 37: Correlation, phase and velocity precision obtained over the Straits of Juan de Fuca. Enough looks were taken so that the pixel size for these estimates was 50 meters  $\times$  50 meters. The L-band velocity precision is about 1 cm/s all from near-range to far-range. The C-band radar, with a much lower transmit power and signal-to-noise ratio, achieves about 2–4 cm/s velocity precision in the near range, but this rapidly worsens with range to as much as 12 cm/s in the far range.

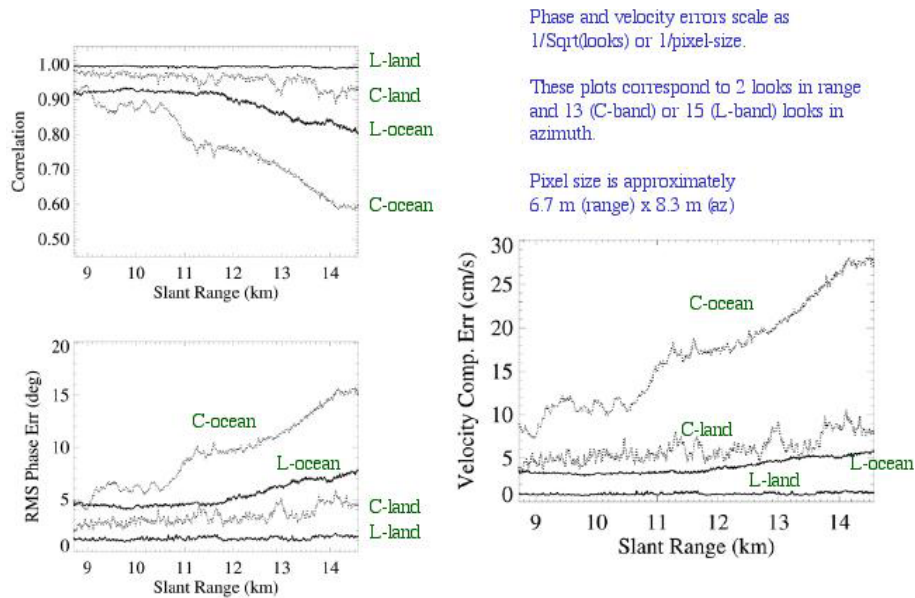


Figure 38: Correlation, phase and velocity precision graphs similar to those of Figure 37, except that many fewer looks were taken, so that the pixel size (which when projected onto the ground varies with slant-range) is about 7 meters  $\times$  8 meters. Also, for this scene the precision is plotted over land as well as over open ocean. With a much higher scattering cross-section, the C-band precision falls off at far-range much less rapidly over land than it does over the ocean. Here, for this pixel size, the L-band velocity precision is about 5 cm/s, while that of C-band varies from 10 cm/s in the near-range to almost 30 cm/s in the far-range.

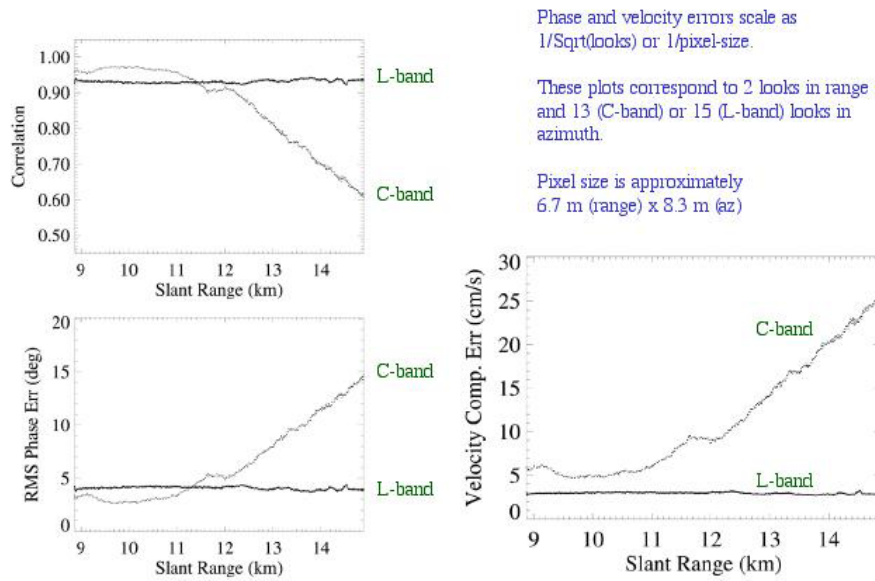


Figure 39: Same graphs as those shown in Figure 38 for the Yakushima205-1, Japan ATI data lines. (Same number of looks and pixel size.) There is, however, no land in this scene, so the comparisons are only for the open ocean. Here, the L-band ATI velocity precision is about 3 cm/s, while that of C-band varies from 5 cm/s in the near-range to about 25 cm/s in the far range.

## 6 Conclusion

The AIRSAR instrument has been upgraded in recent years with more accurate motion-measurement system which, combined with a new higher-accuracy ATI processor has allowed the acquisition, calibration, processing and delivery of a significant number of ATI data sets. We have evaluated the performance of the instrument and the processor, and find that the interferometric alignment is better than 0.1 single-look pixels, and that velocity component precision of 1 cm/s can be achieved at L-band. The velocity component precision at C-band is substantially worse because of the lower transmit power and signal-to-noise ratio at C-band.

### 6.1 Near-Term Outlook

Still to be completed for the calibration of the ATI data is the removal of the absolute phase offset between the two interferometric channels. This should be possible with the use of the caltone phase injected into the receive chain to correct for any gain or phase variations.

Now that geo-location has been added to the ATI processor, another data product which conceivably could be generated is a "Vector ATI" product, where different (parallel) processing of the same data to different look directions leads to estimates of the component of the motion perpendicular to the look direction to the radar, as well as parallel, at the expense of azimuth resolution.

### 6.2 Experimental ATI Modes

In addition to the standard vertically polarized ATI product, there are other polarization channels available to AIRSAR for ATI data collection: at L-band, ATI data can be collected in either HH polarization (transmit horizontally polarized, receive horizontally polarized) or VV polarization. At C-band, in addition to the VV channel VH and HV (i.e., cross-polarized) channels are available.

AIRSAR will be upgraded in FY'02-03 with a new digital system which should allow the addition of new receive channels. One of the ways we hope to make use of this new system is to develop single-pass polarimetric interferometry. This could include polarimetric along-track interferometry, which may be of interest for observing wave-breaking events, or simultaneous cross-track and along-track interferometry, which may help in calibration and in removing the topography phase described in this paper.

#### *Acknowledgement*

The research described in this paper was carried out by the Jet Propulsion Laboratory, California Institute of Technology, under a contract with the National Aeronautics and Space Administration. I wish to acknowledge helpful discussions about algorithm ideas and implementation with Scott Hensley, Ernesto Rodríguez and Paul Rosen. Elaine Chapin and Brian Pollard helped with debugging the processor at several stages in its development. Finally, thanks to Lori Carrico (for ATI data requests), Ellen O'Leary (for planning the

ATI lines used to develop the processor) and to the AIRSAR data acquisition team, without whom we would have no AIRSAR ATI data.

## References

- [Ainsworth et al., 1995] Ainsworth, T., Chubb, S., Fusina, R., Goldstein, R., Jansen, R., Lee, J., and Valenzuela, G. (1995). INSAR imagery of surface currents, wave fields, and fronts. *IEEE Trans. Geoscience and Rem. Sens.*, 33(5):1117–1123.
- [Bau and Alpers, 1999] Bau, M. and Alpers, W. (1999). A new nonlinear integral transform relating ocean wave spectra to phase image spectra of an along-track interferometric synthetic aperture radar. *IEEE Trans. Geoscience and Rem. Sens.*, 37(1):461–466.
- [Carande, 1994] Carande, R. (1994). Estimating ocean coherence time using dual-baseline interferometric synthetic aperture radar. *IEEE Trans. Geoscience and Rem. Sens.*, 32(4):846–854.
- [Curlander and McDonough, 1991] Curlander, J. and McDonough, R. (1991). *Synthetic Aperture Radar: Systems and Signal Processing*. Wiley-Interscience.
- [Elachi, 1988] Elachi, C. (1988). *Spaceborne Radar Remote Sensing: Applications and Techniques*. IEEE Press, New York.
- [Goldstein and Barnett, 1989] Goldstein, R. and Barnett, T. (1989). Remote sensing of ocean currents. *Science*, 246:1282–1285.
- [Goldstein et al., 1994] Goldstein, R., Li, F., Smith, J., Pinkel, R., and Barnett, T. (1994). Remote sensing of ocean waves: The surface wave process program experiment. *J. Geophys. Res.*, 99(C4):7945–7950.
- [Goldstein and Zebker, 1987] Goldstein, R. and Zebker, H. (1987). Interferometric radar measurement of ocean surface currents. *Nature*, 328(20):707–709.
- [Goldstein et al., 1988] Goldstein, R., Zebker, H., and Werner, C. (1988). Satellite radar interferometry: Two-dimensional phase unwrapping. *Radio Science*, 23(4):713–720.
- [Hasselman et al., 1985] Hasselman, K., Raney, R., W.J., P., Alpers, W., Shuchman, R., Lyzenga, D., Ruffenach, C., and Tucker, M. (1985). Theory of synthetic aperture radar ocean imaging: a MARSEN view. *J. Geophys. Res.*, 90(C3):4659–4686.
- [Kasilingam and Shemdin, 1988] Kasilingam, D. and Shemdin, O. (1988). Theory for synthetic aperture radar imaging of the ocean surface: with an application to the tower ocean wave and radar dependence experiment on focus, resolution, and wave height spectra. *J. Geophys. Res.*, 93(C11):13,837–13,848.

- [Kasilingam and Shemdin, 1990] Kasilingam, D. and Shemdin, O. (1990). Models for synthetic aperture radar imaging of the ocean: a comparison. *J. Geophys. Res.*, 95(C9):16,263–16,276.
- [Keller and Plant, 1990] Keller, W. and Plant, W. (1990). Evidence of bragg scattering in microwave doppler spectra of sea return. *J. Geophys. Res.*, 95(C9):16,299–16,310.
- [Lyzenga, 1988] Lyzenga, D. (1988). An analytic representation of the synthetic aperture radar image spectrum for ocean waves. *J. Geophys. Res.*, 93:13,859–13,865.
- [Madsen et al., 1993] Madsen, S., Zebker, H., and Martin, J. (1993). Topographic mapping using radar interferometry: processing techniques. *IEEE Trans. Geoscience and Rem. Sens.*, 31(1):246–256.
- [Madsen, 1989] Madsen, S. N. (1989). Estimating the doppler centroid of sar data. *IEEE Trans. Aero. Electr. Sys.*, AES-25(2):134–140.
- [Marom et al., 1990] Marom, M., Goldstein, R., Thornton, E., and Shemer, L. (1990). Remote sensing of ocean wave spectra by interferometric synthetic aperture radar. *Nature*, 345(28):793–795.
- [Marom et al., 1991] Marom, M., Shemer, L., and Thornton, E. (1991). Energy density directional spectra of nearshore wave field measured by interferometric synthetic aperture radar. *J. Geophys. Res.*, 96(C12):22,125–22,134.
- [Phillips, 1977] Phillips, O. (1977). *The Dynamics of the Upper Ocean*. Cambridge University Press.
- [Raney and Vachon, 1988] Raney, R. and Vachon, P. (1988). Synthetic aperture radar imaging of ocean waves from an airborne platform: focus and tracking issues. *J. Geophys. Res.*, 93:12,475–12,487.
- [Rodríguez and Martin, 1992] Rodríguez, E. and Martin, J. M. (1992). Theory and design of interferometric synthetic aperture radars. *IEE Proc.-F*, 139(2):147–159.
- [Shemer, 1995a] Shemer, L. (1995a). An analytical presentation of the monochromatic ocean wave image by a regular or an interferometric synthetic aperture radar. *IEEE Trans. Geoscience and Rem. Sens.*, 33(4):1008–1013.
- [Shemer, 1995b] Shemer, L. (1995b). On the focusing of ocean swell images produced by a regular and by an interferometric SAR. *Int. J. Remote Sensing*, 16(5):925–947.
- [Shemer and Kit, 1991] Shemer, L. and Kit, E. (1991). Simulation of an interferometric synthetic aperture imagery of an ocean system consisting of a current and a monochromatic wave. *J. Geophys. Res.*, 96(C12):22,063–22,073.

- [Shemer and Marom, 1993] Shemer, L. and Marom, M. (1993). Estimates of ocean coherence time by an interferometric SAR. *Int. J. Remote Sensing*, 14(16):3021–3029.
- [Shemer et al., 1993] Shemer, L., Marom, M., and Markman, D. (1993). Estimates of currents in the nearshore ocean region using synthetic aperture radar. *J. Geophys. Res.*, 98(C4):7001–7010.
- [Thompson and Jensen, 1993] Thompson, D. and Jensen, J. (1993). Synthetic aperture radar interferometry applied to ship-generated internal waves in the 1989 Loch Linhe experiment. *J. Geophys. Res.*, 98(C6):10,259–10,269.
- [Touzi, 1999] Touzi, R. (1999). Coherence estimation for sar imagery. *IEEE Trans. Geoscience and Rem. Sens.*, 37(1):135–149.
- [Tsang et al., 1985] Tsang, L., Kong, J., and Shin, R. (1985). *Theory of Microwave Remote Sensing*. Wiley-Interscience, New York.
- [Vachon, 1999] Vachon, P. (1999). Validation of along-track interferometric sar measurements of ocean surface waves. *IEEE Trans. Geoscience and Rem. Sens.*, 37(1):150–162.
- [van Zyl et al., 1993] van Zyl, J., Chapman, B., Dubois, P., and Shi, J. (1993). The effect of topography on SAR calibration. *IEEE Trans. Geoscience and Rem. Sens.*, 31(5):1036–1043.
- [Zebker and Villasenor, 1992] Zebker, H. and Villasenor, J. (1992). Decorrelation in interferometric radar echoes. *IEEE Trans. Geoscience and Rem. Sens.*, 30(5):950–959.